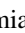








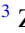
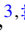




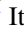




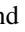



Ambient- and high-pressure studies of structural, electronic, and magnetic properties of single-crystal EuZn_2P_2

Damian Rybicki ^{1,*}, Kamila Komędera ^{1,2}, Janusz Przewoźnik ¹, Łukasz Gondek ¹, Czesław Kapusta ¹, Karolina Podgórska ¹, Wojciech Tabiś ¹, Jan Zukrowski ¹, Lan Maria Tran ^{3,†}, Michał Babij ³, Zbigniew Bukowski ^{3,‡}, Ladislav Havela ^{4,§}, Volodymyr Buturlim ⁴, Jiri Prchal ⁴, Martin Divis ⁴, Petr Kral ⁴, Ilya Turek ⁴, Itzhak Halevy ⁵, Jiri Kastil ⁶, Martin Misek ⁶, Utpal Dutta ⁶ and Dominik Legut ^{4,7}

¹AGH University of Krakow, Faculty of Physics and Applied Computer Science, al. A. Mickiewicza 30, 30-059 Kraków, Poland

²Mössbauer Spectroscopy Laboratory, University of the National Education Commission, ul. Podchorążych 2, 30-084 Krakow, Poland

³Institute of Low Temperature and Structure Research, Polish Academy of Sciences, Okólna 2, 50-422 Wrocław, Poland

⁴Charles University, Faculty of Mathematics and Physics, Department of Condensed Matter Physics, Ke Karlovu 3, 121 16 Prague 2, Czech Republic

⁵Unit of Nuclear Engineering, Faculty of Engineering Science, Ben-Gurion University of the Negev, Be'er Sheva, Israel

⁶Institute of Physics, Academy of Science of the Czech Republic, Na Slovance 1999/2, 182 00 Prague 8, Czech Republic

⁷VŠB - Technical University of Ostrava, IT4Innovations, 17. listopadu 2172/15, 70800 Ostrava, Czech Republic



(Received 26 March 2024; revised 11 June 2024; accepted 17 June 2024; published 12 July 2024)

A thorough study of EuZn_2P_2 single crystals, which were grown from Sn flux, was performed using both bulk (heat capacity, ac susceptibility, dc magnetization, electrical resistivity, magnetoresistance) and microscopic (Mössbauer spectroscopy) techniques. Electrical resistance and magnetic susceptibility were measured also under high pressure conditions (up to 19 and 9.5 GPa, respectively). Further insight into electronic properties and phonons is provided by *ab initio* calculations. The results indicate that EuZn_2P_2 is an antiferromagnet with strong Eu-Eu exchange coupling of ferromagnetic type within the basal plane and weaker antiferromagnetic interaction along the *c* axis. The Eu magnetic moments are tilted from the basal plane. Hydrostatic pressure strongly affects both magnetic (increase of the Néel temperature) and electronic (suppression of the band gap and semimetallic behavior) properties, indicating a strong interplay of structure with magnetic and electronic degrees of freedom.

DOI: [10.1103/PhysRevB.110.014421](https://doi.org/10.1103/PhysRevB.110.014421)

I. INTRODUCTION

Zintl-like phases can be seen as compounds of an electropositive cation, which donates valence electrons to form a framework of covalently bonded polyatomic anions with a closed valence shell. Because of the nature of the chemical bonding, Zintl phases are located at the borderline between valence compounds, which are typical insulators, and the intermetallic compounds, which are typical metals. Often exhibiting intermediate properties, Zintl phases are typically narrow band gap semiconductors. The concept of Zintl like phases was stretched over the periodic table of elements and many Zintl compounds containing *d* and *f* metals are reported in the literature. The situation of a tunable narrow band gap is interesting for practical reasons, as it gives, e.g., prominent thermoelectric properties [1].

A specific situation providing an excellent opportunity of well-defined anisotropy of magnetic and transport properties is offered by the trigonal structure of the CaAl_2Si_2 type (space group No. 164, $P\bar{3}m1$), built by alternating cationic (Ca) and anionic (Al-Si) layers [2]. Incorporating magnetic atoms (e.g.,

Eu) in such a compound gives an intriguing opportunity to explore interplay of magnetic degrees of freedom and electronic structure. In particular, magnetic moments reorientation (in magnetically ordered state), or disordering (in the paramagnetic state) are interesting routes of tuning the band gap width and character of the electronic structure. Properties of Eu-based materials from this family can be further affected by application of the external pressure, which can result in (i) increase of magnetic ordering temperatures, (ii) change of the type of magnetic order (antiferromagnetic to ferromagnetic), (iii) change of the type of the crystal structure, or (iv) insulator to metal transition [3–5].

Recently one of such compounds, EuZn_2P_2 , in which spin magnetic moments of Eu^{2+} ions ($\mu_{\text{sat}}^{\text{th}} = gJ = 7\mu_{\text{B}}$, with $g = 2$ and $J = 7/2$) interact to form an antiferromagnetic state below the Néel temperature $T_{\text{N}} = 23$ K, has been intensively investigated [6–8]. Its magnetic moments were assumed to order ferromagnetically in the basal-plane sheets with Eu^{2+} moments perpendicular to the *c* axis, and the coupling of the neighbor sheets being weaker antiferromagnetic [6]. The stronger ferromagnetic (F) interaction brings a positive paramagnetic Curie temperature $\theta_p = 41.9$ K recorded for field along the *c* axis. Low electrical conductivity and its thermally activated behavior demonstrates a semiconducting ground state. Based on the absence of conduction electrons needed for Ruderman–Kittel–Kasuya–Yoshida (RKKY) exchange interaction, it was argued that the relatively high T_{N}

*Contact author: ryba@agh.edu.pl

†Contact author: l.m.tran@intibs.pl

‡Deceased.

§Contact author: ladislav.havela@matfyz.cuni.cz

is due to a dipolar interaction. The fact that T_N is the highest among the known EuZn_2X_2 compounds (where $X = \text{P, As, Sb}$, see Ref. [6], and citations therein) is given in the context of the smallest lattice volume. The suggested dipole-dipole interaction is, however, to our view unlikely to yield T_N exceeding $T = 20$ K. Moreover, the conductivity was not studied to low enough temperatures to show its possible interplay with the magnetic order.

In Ref. [7], exchange interactions were analyzed and it was concluded that the superexchange mechanism including the P states is the plausible source of the ferromagnetic coupling within the basal-plane sheets.

In the more recent study [8], it was found that the Eu moments indeed order ferromagnetically in layers with the $(+ - + -)$ coupling along the c axis, but they are tilted from the basal plane by $\approx 40^\circ$. It was also shown that a colossal magnetoresistance effect (CMR) appears from the ordered region to temperatures far exceeding T_N .

Our work concentrates on thorough investigation of structural, magnetic, and electronic properties of single crystals at ambient conditions as well as under hydrostatic pressure, which gradually increases the Néel temperature and reduces the electron gap width. The ^{151}Eu Mössbauer spectroscopy and magnetic properties measurements at ambient pressure confirm that the Eu moments are indeed inclined from the basal plane. We also present results of *ab initio* calculations of the lattice dynamics and their implications for the heat capacity analysis.

II. METHODS

Single crystals of EuZn_2P_2 were grown by a Sn flux method in analogy with the process used for EuZn_2As_2 [9]. Typical size of the crystals were $(2 \times 2 \times 0.2)$ mm (see Ref. [10]). Powder x-ray diffraction (XRD) measurements were made by a Panalytical Empyrean diffractometer. For the low-temperature XRD studies an Oxford Instruments Phenix closed-cycle helium refrigerator was used (14–300 K). During the measurements the sample position was corrected against thermal displacement of the sample stage. The stabilization of temperature was better than 0.1 K. The XRD patterns were refined using the Rietveld-type package FULLPROF [11].

The dc magnetization and ac magnetic susceptibility were measured in the temperature range 2–300 K in external magnetic fields $\mu_0 H$ up to 9 T using VSM or ACMS option of a Quantum Design Physical Property Measurement System (PPMS-9). The ac susceptibility was measured using the ac driving field of 1 mT with frequency of 1111 Hz. In none of the methods we applied any demagnetization field correction, which could be difficult due to the irregular sample shapes. However, one should consider that the demagnetization field can have a substantial impact for the $H \parallel c$ geometry.

The heat capacity measurements were carried out by a two- τ relaxation method with the heat capacity options of a Quantum Design Physical Property Measurement System (PPMS-9) in the temperature range 1.85–296 K. The sample for heat capacity measurements was attached and thermally coupled to the addenda with Apiezon N grease. A background signal from addenda and grease (versus T) was recorded, as well.

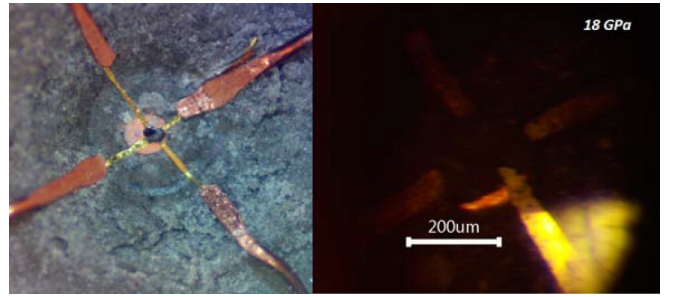


FIG. 1. Arrangement of the contacts for high-pressure resistivity measurements in DAC (left). The picture on the right shows the enlarged detail of the sample at $p = 18$ GPa.

The temperature dependence of electrical resistivity $\rho(T)$ at ambient pressure was measured in the PPMS cryostat (Quantum Design) with Keithley 6517 electrometer in the Alternating Polarity Resistance mode. The temperature range 2–300 K was covered in zero magnetic field. In addition, measurements in applied magnetic fields of 0.1 and 1 T were performed at low temperatures. Electrical contacts were realized by $25 \mu\text{m}$ AlSi wires attached by ultrasonic bonding (HB10 TPT wire bonder). Contact points were arranged within the ab plane in a straight line with a middle point connected to source high output and the outer contacts kept at low potential (ground). The sample resistance in the measured temperature and field range changed by several orders of magnitude, which required changes of the electrometer voltage source settings, each change affecting somewhat the absolute resistivity values. The high temperature region (above 135 K) was measured also by means of the Quantum Design Electrical Transport Option.

The $\rho(T)$ measurements under applied pressure up to 3 GPa were accomplished by means of the Electrical Transport Option with colloidal silver paste and gold wires providing electrical contacts. The geometrical arrangement was equivalent to the ambient pressure measurement. The double-wall pressure cell with a nominal maximum pressure of 3 GPa [12] was used to apply the hydrostatic pressure. The Daphne oil 7474 [13,14] was used as the pressure transmitting medium. The pressure was determined at room temperature from the change of resistance of a thermally stabilized manganese wire. To minimize the thermal gradient during the measurement with pressure cell the rate of temperature change was 0.5 K/min and all curves were measured as zero field cooled (ZFC). The pressure range above 3 GPa was probed using diamond anvil cell (DAC) with NaCl quasihydrostatic pressure transmitting medium. The pressure was measured by shift of ruby fluorescence and the electrical contacts were realized by four gold foils arranged in Van der Pauw configuration (see Fig. 1). This arrangement allowed us to calculate the absolute resistivity in the final high pressure metallic state. The great attention was paid to careful orientation of the samples. After orientation by x-ray diffraction the sample for DAC measurement was polished to $10 \mu\text{m}$ and piece of approximate size of $200 \mu\text{m} \times 150 \mu\text{m}$ was inserted into the sample space of CuBe gasket insulated on one side by alumina filled epoxy.

Magnetization under high pressures has been measured in a SQUID magnetometer (MPMS XL, Quantum Design) using

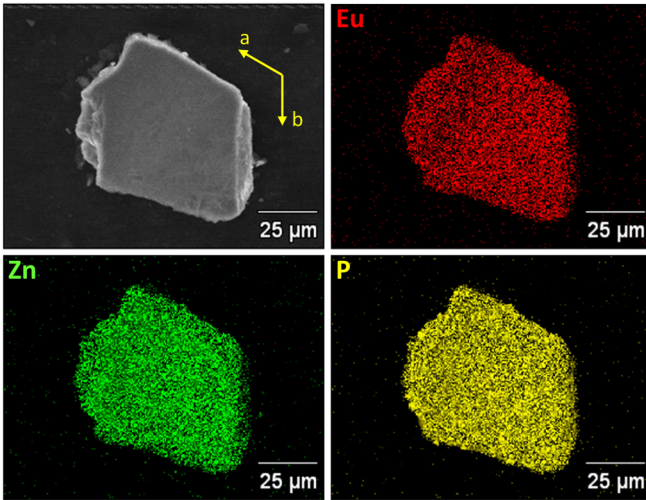


FIG. 2. SEM micrograph of a selected EuZn_2P_2 crystal with individual elemental maps provided by x-ray microanalysis.

miniature diamond anvil pressure cell made of non-magnetic CuBe alloy [15]. Daphne 7474 has been used as the pressure transmitting medium, with a ruby as a manometer. A microgram quantity of the sample has been used with approximate orientation of field parallel to the c axis. Measurement of empty cell without sample has been used as a reference to subtract the background signal of the pressure cell.

^{151}Eu Mössbauer spectra were recorded at 300, 30, and 4.2 K with a conventional constant acceleration spectrometer using the $^{151}\text{Sm}(\text{SmF}_3)$ source. The 21.5 keV γ rays were detected with a NaI(Tl) scintillation detector. The absorber surface density was $\approx 60 \text{ mg/cm}^2$. The spectra were analyzed by means of a least squares fitting procedure. The absorption line positions and relative intensities were calculated by numerical diagonalization of the full hyperfine interactions Hamiltonian. The isomer shift δ is given relative to the $^{151}\text{Sm}(\text{SmF}_3)$ source at room temperature.

The lattice dynamics calculations were done within the direct method [16], as implemented in the PHONOPY code [17], using the $2 \times 2 \times 2$ supercell with the displacement of 0.025 Å. The Hellman-Feynman forces were obtained within the VASP code and in order to minimize the error we use displacements (in total 6) with plus and minus direction. The k -point grid was reduced to $6 \times 6 \times 3$ as this keeps the same density of k -points as for the unit cell. As EuZn_2P_2 is an insulator we included the LO-TO splitting by non-analytical correction [18] by calculating the static dielectric constant ϵ_0 and Born effective charges within the linear response methods as is implemented in the VASP code, yielding the values of $\epsilon_0 = 18.885/17.853$ and $Z^* = 4.17/5.44, 0.24/-0.41, \text{ and } -2.32/-2.30$ along x/z direction for Eu, Zn, and P atoms.

III. RESULTS AND DISCUSSION

A. XRD and SEM

Microstructure and composition of the EuZn_2P_2 single crystals were studied by scanning electron microscopy (SEM). An example is shown in Fig. 2. The elemental distribution is homogeneous, as checked for few large crystals and

several small pieces. The overall elemental abundance of Eu 19.4 at.%, Zn 39.6 at.%, P 41.0 at.%, was found, which is in a good agreement with theoretical stoichiometry. The trigonal structure was clearly imprinted onto the crystals morphology with the large flat surfaces representing the basal planes, as checked by x-ray diffraction.

X-ray diffraction (XRD) patterns of EuZn_2P_2 collected in the temperature 15–300 K range can be fully indexed on the basis of the trigonal $P\bar{3}m1$ space group (No. 164). The refined XRD pattern at $T = 15 \text{ K}$ is shown in Fig. 3. The refinement and absence of any spurious phase indicate a good quality of the sample. The lattice parameters obtained are $a = 4.0779(1) \text{ \AA}$, $c = 6.9834(3) \text{ \AA}$ and $a = 4.0866(1) \text{ \AA}$, $c = 7.0066(3) \text{ \AA}$ at $T = 15$ and 300 K, respectively. The values at 300 K are in a good agreement with the previously reported structure data [6]. The most interesting structure features were broadly discussed in our earlier paper concerning the isostructural system EuZn_2As_2 [9].

The temperature dependence of the unit cell volume, presented in Fig. 3(b), could be in the paramagnetic state approximated by the Debye formula [19]:

$$V = V_0 + I_C \frac{T^4}{\theta_D^3} \int_0^{\frac{\theta_D}{T}} \frac{x^3}{e^x - 1} dx, \quad (1)$$

where V_0 is the unit cell volume extrapolated to 0 K, I_C is a slope of the linear part of the $V(T)$ dependent on Grüneisen and compressibility parameters, while θ_D is the Debye temperature. Both $a(T)$ and $c(T)$ (see Ref. [10]) are linear above $\approx 130 \text{ K}$. This allows to evaluate individual linear thermal expansion coefficients $\alpha_a = 1.01 \times 10^{-5} \text{ K}^{-1}$ and $\alpha_c = 1.48 \times 10^{-5} \text{ K}^{-1}$, which gives the volume thermal expansion $\alpha_V = 3.50 \times 10^{-5} \text{ K}^{-1}$. The extrapolated unit cell volume was found to be $V_0 = 100.63(1) \text{ \AA}^3$, $I_C = 0.0119(1) \text{ \AA}^3 \text{ K}^{-1}$, and the Debye temperature $\theta_D = 324(11) \text{ K}$. The Debye temperature is higher than for the analogous arsenide EuZn_2As_2 (261 K) [9], which can be attributed to the difference in atomic mass, leading to the increase of the phonon velocity. At low temperatures, below 40 K, an anomalous behavior of lattice parameters can be related to magnetic phenomena, see Figs. 3(c)–3(e). Namely, both lattice parameters exhibit a sudden drop at $T = 30 \text{ K}$ for the a parameter, and at 24 K for c . The a parameter has a maximum at 20 K, followed by the next drop below 19 K. These features are also reflected in $V(T)$ [Fig. 3(e)] as two steps at 30 and 20 K, respectively. Throughout all the T range, the internal structure parameters determining the position of the Zn and P atoms are invariable within the experimental uncertainty.

B. Heat capacity measurements

Temperature dependence of the specific heat (C_p) as well as its magnetic part (C_{mag}) are shown in Fig. 4. One can notice a sharp peak at $T = 23.3 \text{ K}$, which reflects critical temperature of the antiferromagnetic ordering (Néel temperature T_N) of the Eu^{2+} moments. Due to the absence of crystal-field phenomena for spherically symmetric $4f^7$ state, no magnetic entropy should be present sufficiently far above T_N . In the absence of electronic heat capacity, the paramagnetic $C_p(T)$ is given by the lattice contribution. In the simple approach, we approximate it using a convenient mix of acoustic and optical

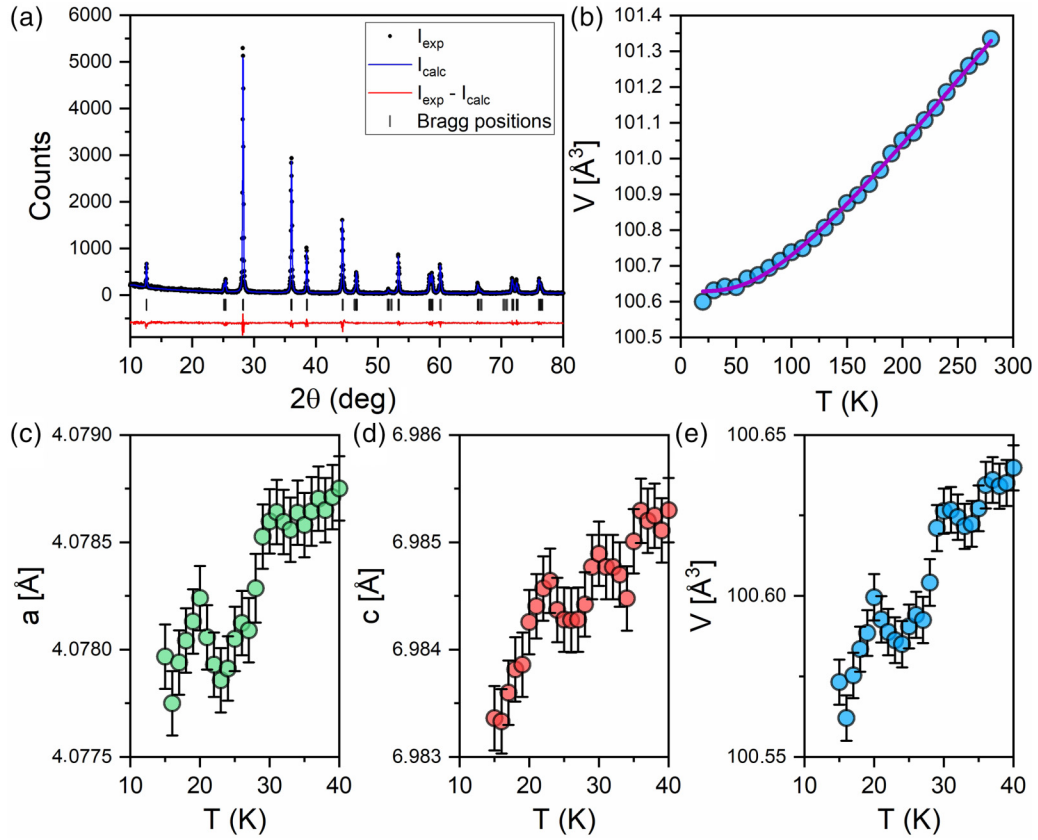


FIG. 3. Results of x-ray diffraction studies in the temperature range 15–300 K: Rietveld refinement of diffraction pattern collected at 15 K (a), unit cell volume in entire experimental range with fitted Debye curve (b), low temperature behavior of individual lattice parameters [(c) and (d)], and unit cell volume (e).

phonons, with characteristic temperatures obtained by guess and fit method. We assume that such a function is valid even in the magnetic state, which allows us to extract the magnetic heat capacity and magnetic entropy. In particular, we used the

expression:

$$C_{\text{ph}} = \frac{R}{1 - \alpha T} \left[9 \left(\frac{T}{\theta_D} \right)^3 \int_0^{\frac{\theta_D}{T}} \frac{x^4 e^x}{(e^x - 1)^2} dx + \sum_i \frac{m_i \left(\frac{\theta_{E_i}}{T} \right)^2 e^{\theta_{E_i}/T}}{(e^{\theta_{E_i}/T} - 1)^2} \right], \quad (2)$$

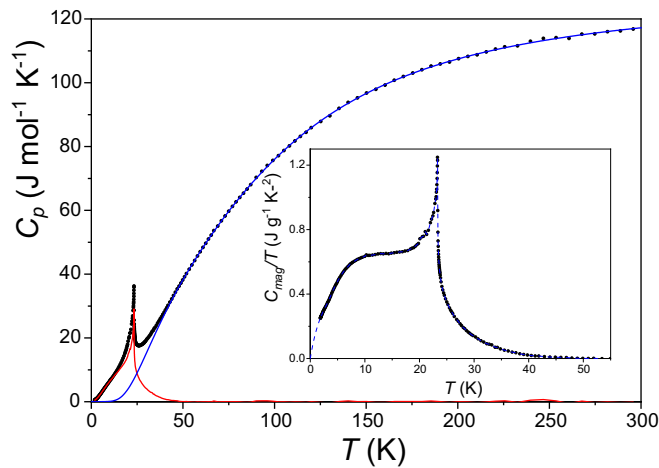


FIG. 4. Temperature dependence of the measured specific heat C_p (black). The solid blue line is a fit by Eq. (2) and the solid red line is the calculated magnetic contribution C_{mag} to the heat capacity. The inset shows C_{mag}/T as a function of T . The dashed line in the inset is an extrapolation of the data to $T = 0$ K and the guide to the eye at higher T .

where θ_D is the Debye temperature, θ_{E_i} are Einstein temperatures with m_i as corresponding multiplicities for each individual optical branch, α stands for an anharmonic coefficient, and R is the universal gas constant [20,21]. In the recent reports [6,8], a model with two Debye temperatures was proposed, but our model describes the experimental data better. In order to facilitate the analysis, the summation over 12 independent optical branches was grouped into 2 branches with sixfold degeneracy. The fit to the experimental data was done in the temperature range from 48 to 296 K, i.e., far from the T_N , and it is represented by the solid blue curve in Fig. 4. The obtained fitting parameters are summarized in Table I. One can notice that the Debye temperature obtained, $\theta_D = (277 \pm 8)$ K, is in a reasonable agreement with estimate obtained from the lattice expansion [(324 ± 11) K]. Previous studies reported $\theta_{D1} = 493$ K and $\theta_{D2} = 182$ K (two-Debye temperatures model) [6] and $\theta_D = 480$ K (Debye and Einstein terms, but in different formula than ours) [7]. We note that if we apply formula from Singh *et al.* we obtain

TABLE I. Debye (θ_D) and Einstein (θ_{E_i}) temperatures and anharmonic coefficient (α) obtained from the fitting of Eq. (2) to the temperature dependence of C_p .

θ_D (K)	277 ± 8
θ_{E_1} (K)	130 ± 2
θ_{E_2} (K)	406 ± 2
α (1/K)	$(3.6 \pm 0.3) \times 10^{-5}$

very similar values to theirs, which indicates that they depend on the model used for the fit of the lattice contribution to the heat capacity. However, $\theta_D = 480$ K seems to be rather high, since in similar Eu containing compounds values not exceeding 330 K were reported [22–27].

The magnetic part of the specific heat

$$C_{\text{mag}}(T) = C_p(T) - C_{\text{ph}}(T) \quad (3)$$

is shown in Fig. 4 as a solid red line. As can be seen, C_{mag} remains finite in a limited range above T_N and vanishes only at temperatures above ≈ 50 K, which is a sign of short range magnetic correlations [23,27].

The magnetic entropy $S_{\text{mag}}(T)$ was calculated from the $C_{\text{mag}}(T)$ using the following formula:

$$S_{\text{mag}}(T) = \int_0^T \frac{C_{\text{mag}}}{T'} dT'. \quad (4)$$

As the measurement was carried out only down to 1.85 K, the C_{mag}/T data were extrapolated from 1.85 to 0 K using a third-order polynomial function (fitted to the low-temperature experimental points). S_{mag} calculated between $T = 0$ and 50 K was determined by numerical integration of the dashed curve shown in the inset in Fig. 4 and is equal to $16.4 \text{ J mol}^{-1} \text{ K}^{-1}$. The expected value of S_{mag} of one mole of particles with spin J in a magnetic field is given by $S_{\text{mag}} = R \ln(2J + 1)$, which for $J = 7/2$ (value for Eu^{2+} ions) amounts to $17.28 \text{ J mol}^{-1} \text{ K}^{-1}$. Our experimental value is somewhat lower than the theoretical one, but much closer than previously reported one ($11.3 \text{ J mol}^{-1} \text{ K}^{-1}$) [6], which is most likely owing to better estimate of the phonon contribution in our model compared to the two-Debye model proposed in Ref. [6]. We note that in many structurally similar antiferromagnetic compounds, S_{mag} at T_N is lower than the expected value [see Figs. 6(c) and 6(g)], which is typically attributed to short range magnetic correlations that appear at temperatures higher than T_N [22–27].

It is interesting to compare such empirical approach (with multiple tunable parameters) with a fundamental parameter-free approach based on *ab initio* calculations of lattice dynamics, which describe phonon dispersion relations including a dispersion in optical modes. Figure 5 shows the calculated phonon dispersion relations and respective densities of phonon states. One can distinguish dominant Eu-based acoustic modes at the lowest energies, followed by Eu optical modes at 10–13 meV. The Zn optical modes extend up to 20 meV. High energy optical modes related to P vibrations are concentrated into the range 30–37 meV. A careful examination reveals an inflexion point in the Eu-based phonon DOS

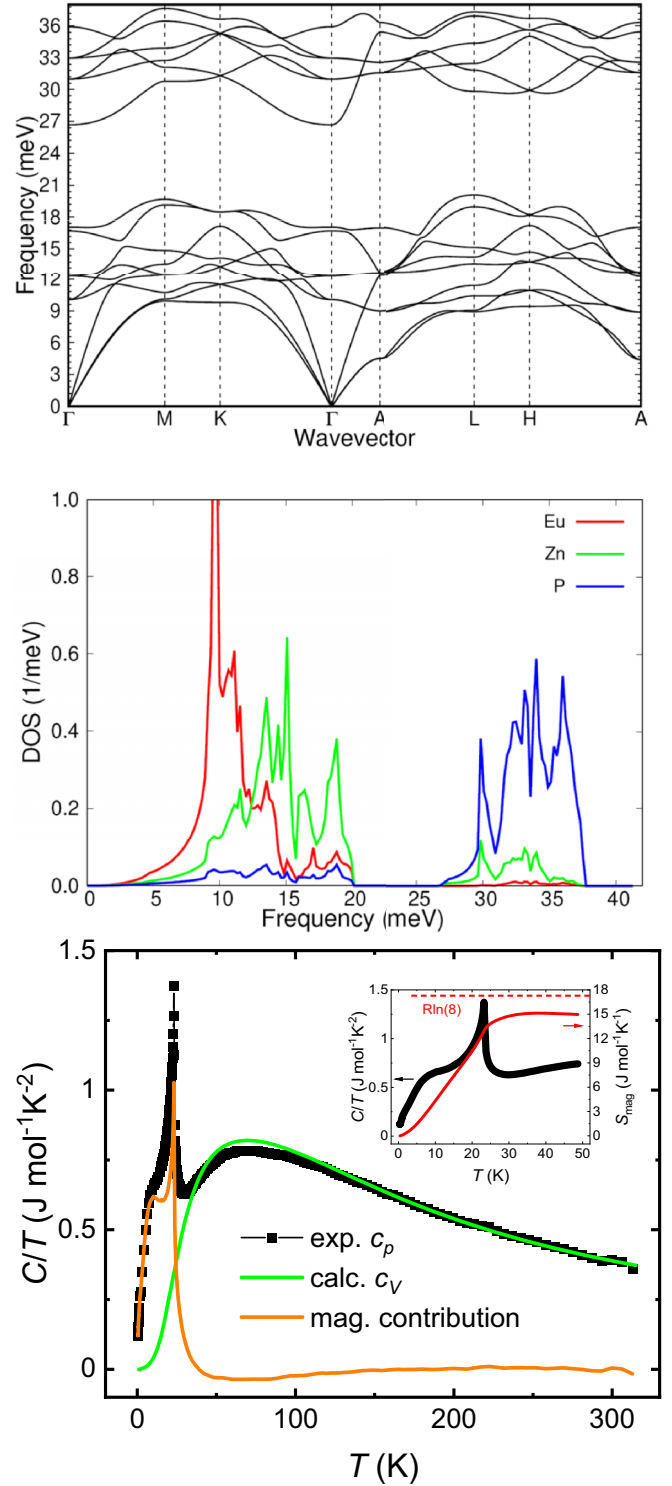


FIG. 5. Calculated phonon dispersion relations (top) and partial phonon densities of states decomposed into contributions of individual elements (middle). The lower panel displays the experimental specific heat C_p data together with theoretical phonon specific heat calculated for constant volume, C_V (green line), used to separate the magnetic contribution C_{mag} (orange line) and magnetic entropy (red line), shown in the inset.

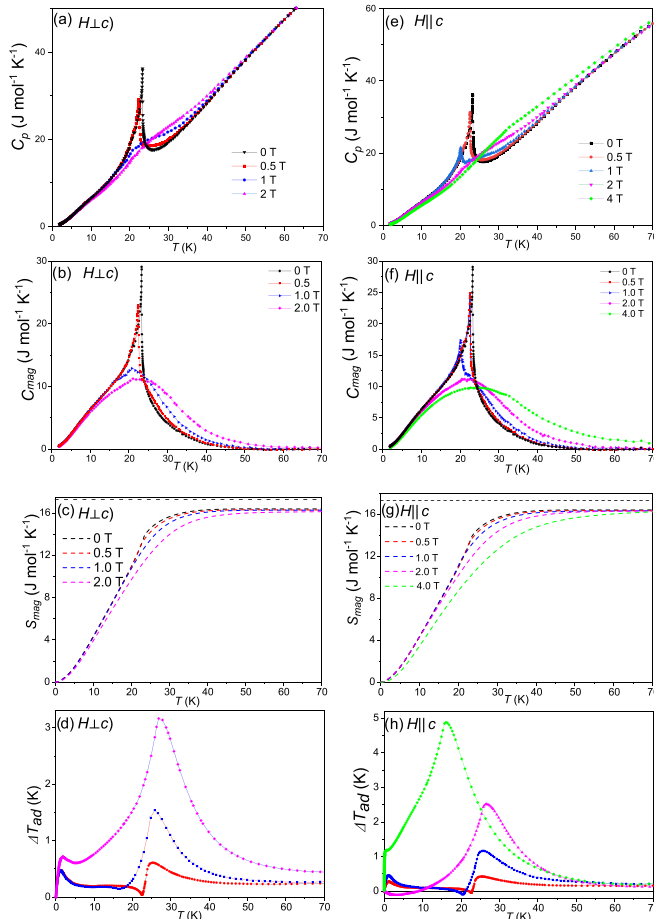


FIG. 6. Temperature and magnetic field dependence of the measured specific heat C_p , for magnetic fields perpendicular and parallel to the c axis in (a) and (e), respectively. (b) and (f) show the magnetic contribution C_{mag} to heat capacity. (c) and (g) show magnetic entropy S_{mag} calculated from the data in the (b) and (f), black dashed lines for $S_{\text{mag}} = 17.28 \text{ J mol}^{-1} \text{ K}^{-1}$ indicate a theoretical value of S_{mag} . (d) and (h) show adiabatic temperature changes ΔT_{ad} as a function of temperature.

at 4 meV. Analysis of individual dispersion relations reveals that below this energy there is rather soft transversal acoustic Eu phonon mode from the Γ to A point of the Brillouin zone, i.e., the mode with the wave vector q along the c axis. As a whole, the phonon spectrum is strongly non-Debye like.

Calculated phonon density of states (DOS) allows to determine a theoretical lattice heat capacity at constant volume C_V displayed in the bottom panel of Fig. 5 as the green line. The remaining nonphononic part of the heat capacity we attribute to the magnetic heat capacity, C_{mag} , and it can be again taken to estimate the magnetic entropy, which is calculated as $15.2 \text{ J mol}^{-1} \text{ K}^{-1}$. Such value is somewhat lower than the previous estimate and hence more below the theoretical limit. Figure 5 reveals a small issue of the lattice specific heat in the 50–80 K range. The experimental data are slightly below the theoretical curve. Above this range the theory and experiment coincide. It suggests that the computations, bound to the $T = 0$ limit, may overestimate the softness of the lattice at low temperatures, which would reduce the calculated mag-

netic entropy in the ordered state. Nevertheless the theoretical phonon DOS gives a justification to the chosen Einstein temperatures given in Table I. The $\theta_{E_1} = 130 \text{ K}$ corresponds to 11.2 meV, roughly in the middle of the energy range of Eu optical phonons, while $\theta_{E_1} = 406 \text{ K}$, i.e., 35 meV, stands for energies of P optical phonons.

Figure 6 shows results of measurements of the heat capacity in magnetic fields, applied parallel to the c axis or perpendicular to it. The sharp peak indicating the second-order phase transition to the antiferromagnetic state, which is clearly visible in zero field, shifts towards lower temperatures, becomes broader and eventually vanishes at fields exceeding the critical field needed for ferromagnetic-like alignment of Eu moments. Higher magnetic fields shift the magnetic entropy towards higher temperatures, in analogy with common ferromagnets. The critical field where the phase transition disappears takes place at lower field for the $H \perp c$ orientation, which is in agreement with the $M(H)$ curves, where the saturation of magnetization (see Fig. 10) happens in lower fields. The behavior of the magnetic contribution C_{mag} , which was calculated after subtracting the lattice contribution approximated with fitted theoretical curve, Eq. (2), is better visible in Figs. 6(b) and 6(f) for both orientations. The $C_{\text{mag}}(T)$ shows features typical for antiferromagnetically ordered Eu compounds [9,23,28], i.e., it shifts towards low temperatures and broadens. The exact temperatures of the peak related to the antiferromagnetic order are shown below in Fig. 12.

We also calculated the magnetic entropy S_{mag} using Eq. (4) and its temperature and field dependencies are shown in Figs. 6(c) and 6(g). For all fields and both orientations, S_{mag} is lower than the theoretical value ($17.28 \text{ J mol}^{-1} \text{ K}^{-1}$) and it saturates at temperatures increasing with applied magnetic fields, reaching $T = 70 \text{ K}$ at our experimental conditions. The release of the entropy above T_N due to short range correlations was observed previously for other Eu compounds [23,25–27]. The collected data allow to calculate an adiabatic temperature change ΔT_{ad} , using the relation:

$$\Delta T_{\text{ad}}(T, \Delta H) = T(S, H_f) - T(S, H_i), \quad (5)$$

where $T(S, H)$ is temperature as a function of the total entropy S and magnetic field H (initial $H_i = 0$ and final $H_f > 0$) [29]. Calculated values of ΔT_{ad} for both field orientations are presented in Figs. 6(d) and 6(h). For $\mu_0 H = 2 \text{ T}$ perpendicular to the c axis, the maximum value of ΔT_{ad} amounts to 3.16 K and is larger compared to 2.52 K value obtained for the $H \parallel c$ orientation, indicating stronger magnetocaloric effect for the $H \perp c$ orientation. For $H \parallel c$ at 4 T the maximum value of ΔT_{ad} almost doubles and amounts to 4.88 K. All these observations are in line with the results obtained for very similar antiferromagnetically ordered EuZn_2As_2 [9]. The maximum values of ΔT_{ad} are also comparable to those obtained for ferromagnetic EuO [30].

C. Magnetic measurements

1. Ac susceptibility

Temperature dependence of ac susceptibility investigated in zero static magnetic field ($\mu_0 H = 0 \text{ T}$) using the ac driving field 1 mT applied perpendicular and parallel to the crystallographic c axis is shown in Fig. 7. As can be seen, the real

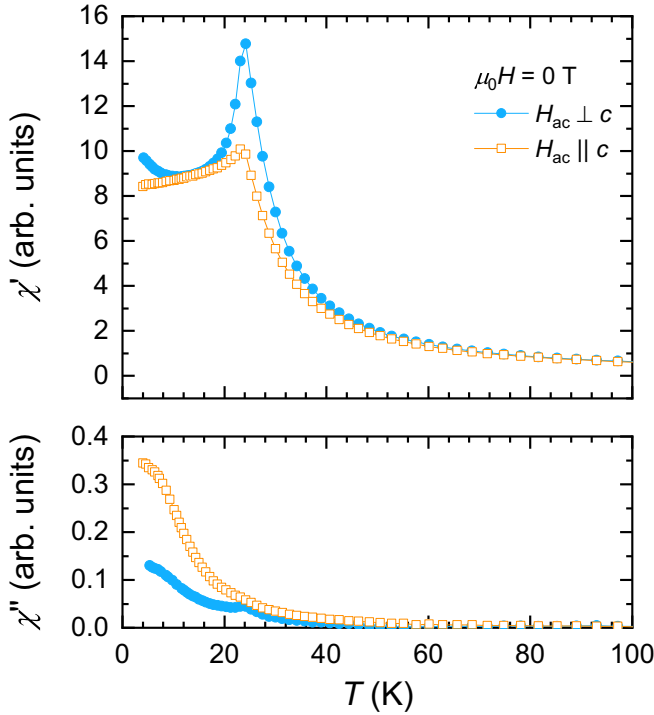


FIG. 7. Real (top) and imaginary (bottom) parts of ac susceptibility investigated with driving field of 1 mT applied perpendicular (closed blue circles) and parallel (open orange squares) to the c axis measured in zero static magnetic field.

part of susceptibility $\chi'(T)$ exhibits a sharp maximum at about 23 K. At the same time a less pronounced maximum can be observed in the imaginary part of susceptibility $\chi''(T)$. As discussed below, these are the fingerprints of the antiferromagnetic transition.

For a typical antiferromagnet with low magnetocrystalline anisotropy, one would expect below T_N to see a decrease of susceptibility for the so called “easy direction” and (nearly) constant values of susceptibility for the other direction. However, EuZn_2P_2 exhibits with decreasing temperature different behavior of $\chi'(T)$. The susceptibility increases for $H_{ac} \perp c$ and for $H_{ac} \parallel c$ it decreases first but a small kink is observed at about 5 K. In addition, the imaginary part of susceptibility $\chi''(T)$ increases (below T_N), which reflects energy dissipation associated with remagnetization in the already magnetic state.

For non-zero external static magnetic fields, additional anomalies are observed for the real and imaginary parts of ac susceptibility in both field directions (see Fig. 8). While the maximum at 23 K (associated with the antiferromagnetic transition) shifts towards the lower temperatures with increasing $\mu_0 H$ for both directions, the shape of $\chi'(T)$ depends on the direction. For $H \perp c$, $\chi'(T)$ below T_N changes to nearly temperature independent (flat type), while for $H \parallel c$ it decreases with decreasing temperatures. For low fields ($\mu_0 H < 0.3$ T) applied perpendicular to the c axis, $\chi'(T)$ exhibits a broad maximum, which is accompanied by a maximum in $\chi''(T)$ below the T_N , but for higher fields the maximum appears above T_N , in other words, this maximum is shifted towards higher temperatures with increasing static magnetic field. On

the other hand, for $H \parallel c$ such maximum in $\chi'(T)$ is visible only for higher fields (0.5 T) and the response in the $\chi''(T)$ is much more subtle than in the $H \perp c$ case. An anomaly that is shifted towards higher temperatures by increasing static magnetic field can be associated with a reorientation of Eu^{2+} magnetic moments towards the field direction. In static fields exceeding 3 T, a ferromagnetic-like alignment is achieved. Hence the ac susceptibility becomes low and practically featureless on the given temperature scale.

Similar behavior (increase for $\mu_0 H = 0$ T and nearly temperature independent $\chi(T)$ for $\mu_0 H > 0$ T) of the real part of susceptibility below T_N for $H_{ac} \perp c$ (and $H \perp c$) was observed for example for EuFe_2As_2 and $\text{Eu}_{0.88}\text{Ca}_{0.12}\text{Fe}_2\text{As}_2$ [10,31]. It was proposed that this is most likely due to the detwinning process, which we can not exclude in the case of EuZn_2P_2 .

On the contrary, the $\chi'(T)$ dependence for $c \parallel \mu_0 H > 0$ T does not resemble susceptibility for the mentioned compounds (see Refs. [10,15,32–42]). We do find, however, some similarities for EuZn_2As_2 [9], as well as for the Co-doped EuFe_2As_2 compounds [43,44]. For all of these compounds, the magnetic moments of Eu^{2+} are tilted from the basal plane.

This can lead us to assumption that also in EuZn_2P_2 the magnetic moments of Eu^{2+} order antiferromagnetically but are tilted from the basal plane, in agreement with the Mössbauer spectroscopy results presented below (see Sec. III D). Moreover, the observed ferromagnetic-like anomaly below the antiferromagnetic transition can be associated with: (i) the detwinning process (or presence of antiferromagnetic domains), (ii) possible spiral order instead of an A-type antiferromagnetic one, which results in existence of an ferromagnetic component, i.e., ferromagnetic interactions between Eu^{2+} magnetic moments.

2. Dc magnetization

Although the dc magnetization of EuZn_2P_2 was studied already [6–8], we performed dc magnetization measurements in a broader range of temperatures and magnetic fields for a more complete description. This also enabled us to draw a more detailed magnetic phase diagram of the investigated system (see Sec. III E).

Temperature dependence of dc magnetic susceptibility investigated at low magnetic fields applied perpendicular ($H \perp c$) and parallel ($H \parallel c$) to the crystallographic c axis, strongly resembling the ac susceptibility data, is shown in Fig. 9(a). It increases with decreasing temperatures until a kink at $T_N \approx 23$ K is reached, and then it decreases.

Temperature dependencies of the inverse susceptibility, $1/\chi$, measured in $\mu_0 H = 9$ T applied perpendicular and parallel to the c axis are shown in Figs. 9(b) and 9(c), respectively. The $1/\chi(T)$ dependence is linear at high temperatures. Fitting the experimental data to the Curie-Weiss law:

$$\chi(T) = \frac{N_A}{3k_B\mu_0} \frac{\mu_{\text{eff}}^2}{T - \theta_p}, \quad (6)$$

where N_A is the Avogadro number, k_B the Boltzmann constant, μ_0 permeability of vacuum, θ_p the paramagnetic Curie temperature, μ_{eff} effective magnetic moment (in Bohr magnetons μ_B) gives $\mu_{\text{eff}}^{\perp c} = (7.74 \pm 0.01) \mu_B$ and $\mu_{\text{eff}}^{\parallel c} = (7.87 \pm 0.01) \mu_B$ for $H \perp c$ and $H \parallel c$, respectively; which

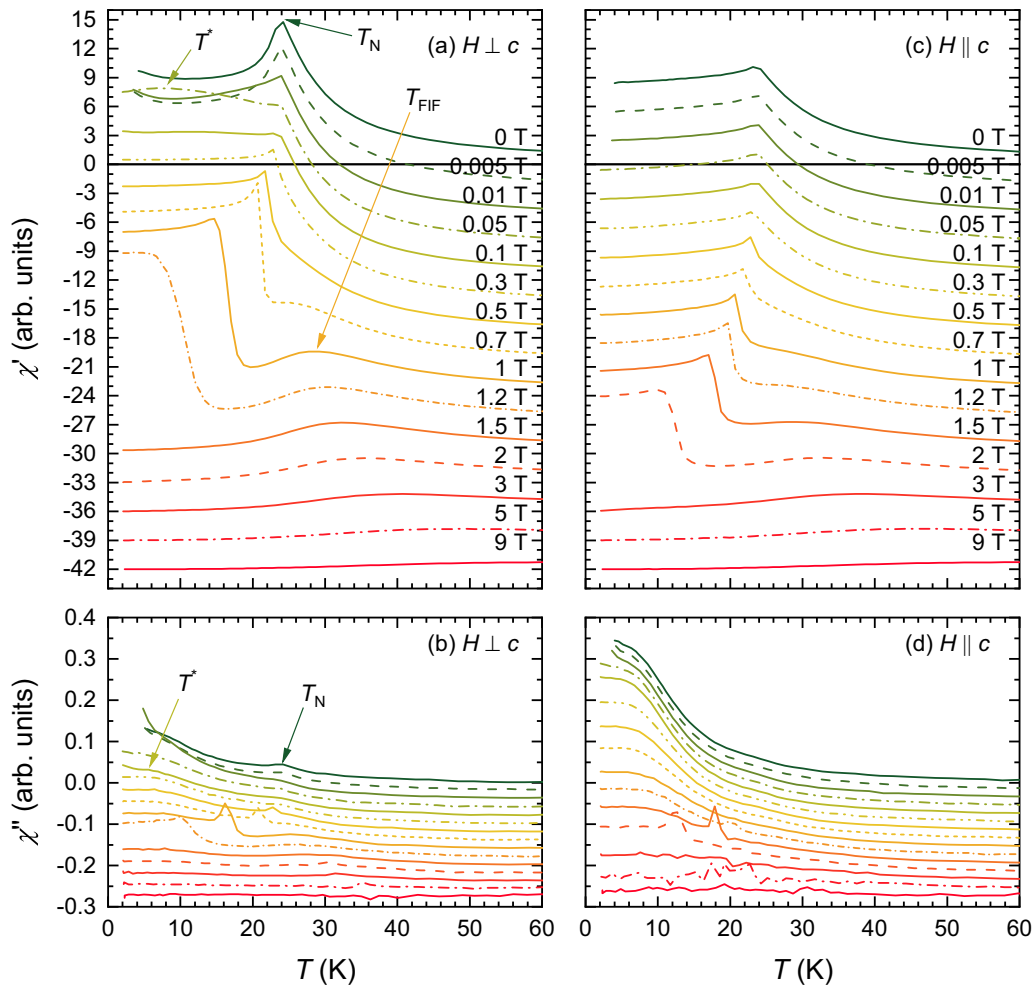


FIG. 8. Real [(a) and (c)] and imaginary [(b) and (d)] parts of ac susceptibility investigated with driving field $H_{ac} = 1$ mT ($f = 1111$ Hz) in various static magnetic fields $\mu_0 H$ applied perpendicular [(a) and (b)] and parallel [(c) and (d)] to the c axis. The dependencies for $\mu_0 H \geq 0.005$ T are shifted along the y axis by 3 in (a) and (c) and by 0.02 in (b) and (d).

is close to $7.94 \mu_B$, the theoretical value for the $4f^7$ configuration. The evaluated paramagnetic Curie temperature, positive for both orientations ($\theta_p^{\perp c} = (27.8 \pm 0.2)$ K and $\theta_p^{\parallel c} = (24.8 \pm 0.3)$ K) indicates that the ferromagnetic

interactions are dominant despite the AF ground state. The above findings are in very good agreement with previous studies on this material [6–8]. The anomaly at T_N shifts towards lower temperatures (see Ref. [10]) with increasing

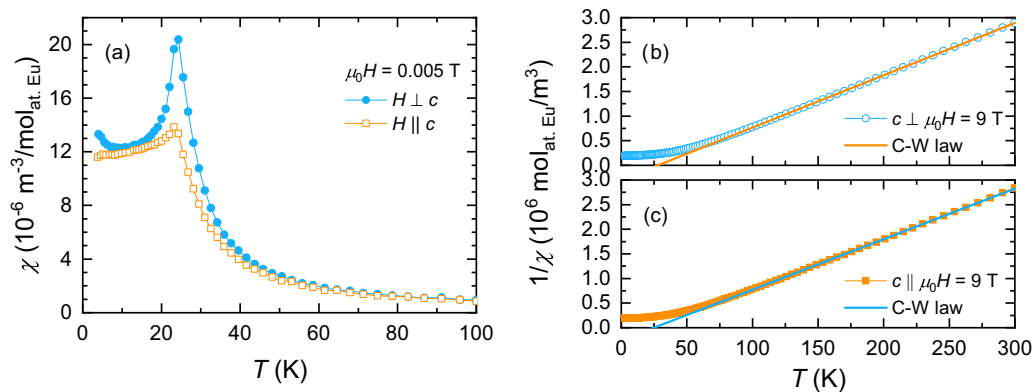


FIG. 9. Temperature dependence of (a) dc magnetic susceptibility χ investigated in $\mu_0 H = 5$ mT applied perpendicular (closed blue circles) and parallel (open orange squares) to the crystallographic c axis, and [(b) and (c)] inverted susceptibility $1/\chi$ measured in $\mu_0 H = 9$ T applied perpendicular [(b), open blue circles] and parallel [(c), closed orange squares] to the crystallographic c axis together with respective fits with the Curie-Weiss law, Eq. (6), between 100 and 300 K (solid lines).

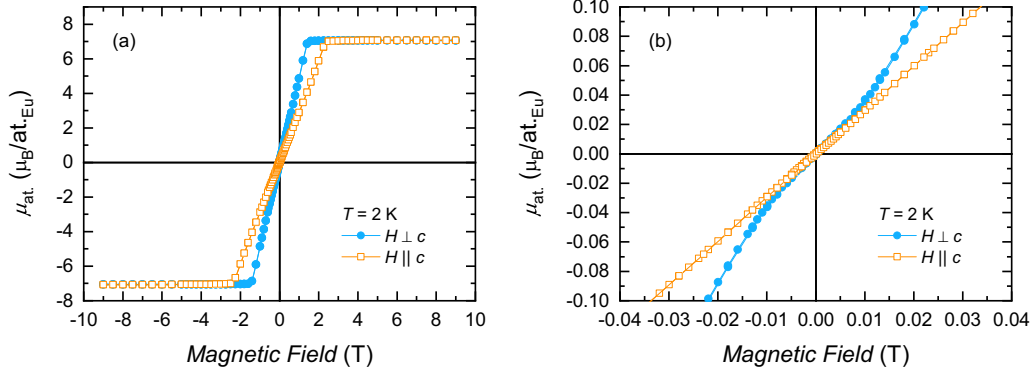


FIG. 10. Magnetic field dependence of the dc magnetization per Eu^{2+} at 2 K for $c \parallel H$ and $c \perp H$ orientations (a) for magnetic fields up to 9 T with an enlarged view of the low field region (b).

external magnetic field H , as usual in antiferromagnets. Field dependencies of magnetization for $H \perp c$ and $H \parallel c$ orientations measured at $T = 2$ K are presented in Fig. 10(a). Both curves show, as expected for an antiferromagnet, no spontaneous magnetization and no magnetic hysteresis. The response in low fields is linear. At sufficiently high fields magnetization for both orientations saturates to $7 \mu_B$ per Eu atom, which is consistent with the theoretical value for Eu^{2+} ($\mu_{\text{sat}}^{\text{th}} = 7 \mu_B$). The field at which saturation is reached depends on the orientation and is equal 1.3 and 2.5 T for $H \perp c$ and $H \parallel c$ orientations, respectively. These fields correspond to a crossover to the field-induced ferromagnetic state, i.e., state at which all magnetic moments of Eu^{2+} align ferromagnetically under the influence of magnetic field.

At very low fields (below 0.02 T), see Fig. 10(b), one can notice that for the $H \perp c$ orientation there is a clear change of behavior of magnetization. It first increases slowly and then from about 0.015 T it starts to increase more rapidly, maintaining the same slope until reaching the saturation. It resembles the virgin magnetization curve of the ferromagnets with domain wall pinning mechanism of the magnetization reversal. The same behavior was found in EuZn_2P_2 by Krebber *et al.* [8], as well as in other Eu containing compounds [26,27,31,45] and was attributed to either the presence of antiferromagnetic domains, which were vanishing at higher fields (above 0.05 T), or the detwinning process. This effect may be related to the presence of three equivalent directions in the unit cell for Eu^{2+} moments tilted from the c axis, which corresponds to its threefold rotational symmetry.

D. Mössbauer spectroscopy measurements

There are very few experimental techniques, which can provide information regarding the orientation of ordered magnetic moments. One of them is Mössbauer spectroscopy and we carried out such measurements on the ^{151}Eu isotope. In Fig. 11, we present results of measurements carried out in the ordered (at $T = 4$ K) and paramagnetic state (30 and 300 K). At the room temperature [Fig. 11(a)], the spectrum consists of a single absorption line with isomer shift $\delta = -11.09$ mm/s, which is typical for Eu^{2+} ions [46–48].

The other parameters, which can be obtained from the fit of experimental data, are the largest component of the electric field gradient tensor (EFG), V_{zz} , and the quadrupole coupling,

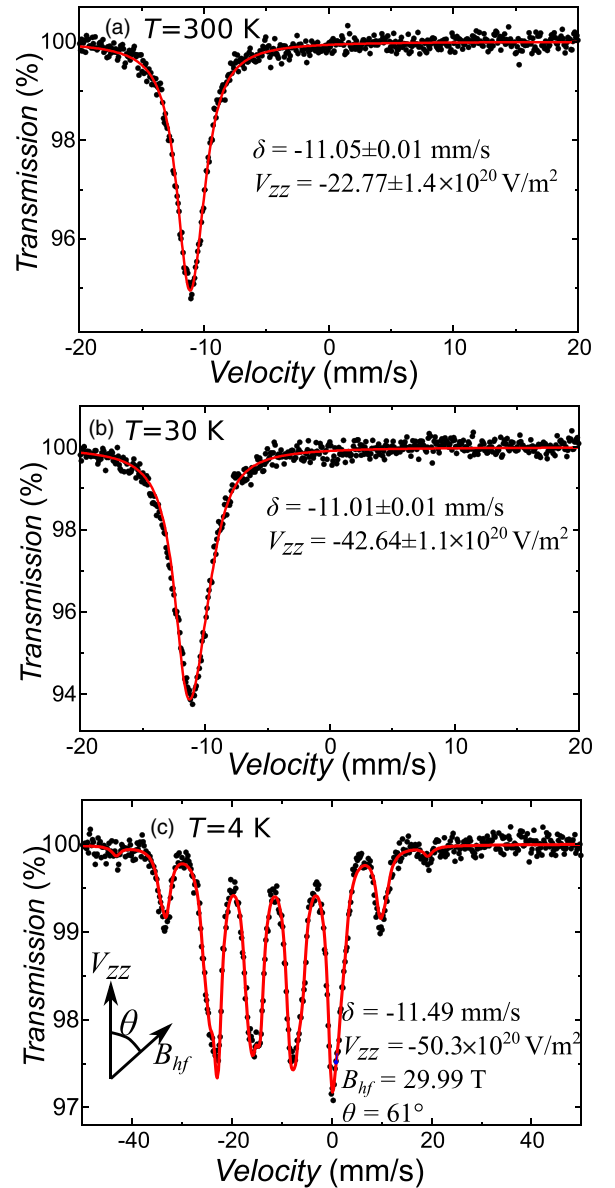


FIG. 11. ^{151}Eu Mössbauer spectra of EuZn_2P_2 measured at (a) room temperature, (b) $T = 30$ and (c) 4 K. Experimental data are shown as black squares and the red line is the result of the fit, which parameters (δ , V_{zz} , B_{hf} and θ) are also provided.

ϵ , which is a result of the interaction of EFG with a nuclear electric quadrupole moment, Q_g . EFG at the Eu site has two sources, the first one is due to its own electrons and the second comes from neighboring ions. The Eu^{2+} ion has a half-filled $4f^7$ electronic configuration with the $^8\text{S}_{7/2}$ ground state, so that the $4f$ electron contribution to the EFG is expected to be zero. The second contribution coming from the “lattice” in our case is also expected to be rather small since the Eu site has a rather high symmetry ($3\bar{m}$ point symmetry). Therefore the EFG, V_{zz} and the resulting quadrupole coupling, ϵ , are expected to be small. Since the c axis is a threefold rotation axis, one expects that it becomes the principal axis of the EFG tensor [49] and the tensor itself is axially symmetric along it, i.e., the V_{zz} component is along the c axis. Then the quadrupole coupling ϵ in the paramagnetic state can be written as:

$$\epsilon = \frac{1}{4} \frac{ceQ_g V_{zz}}{E_\gamma}, \quad (7)$$

where c is the light velocity in vacuum, e electron charge, and E_γ is the Mössbauer photon energy. In the case of ^{151}Eu Mössbauer spectroscopy one can learn the sign of V_{zz} in the paramagnetic state from the asymmetry of the spectrum. The tail towards more negative (positive) values of the velocity indicates a positive (negative) sign of V_{zz} . In our case V_{zz} is small so it is difficult to distinguish its sign just by the eye. Therefore we calculated the skewness and determined its positive sign, meaning a negative sign of V_{zz} . From the fit to the data at $T = 300$ K, we obtain $V_{zz} = -22.8 \times 10^{20}$ V/m², which is comparable to the value for EuZn_2As_2 [9] and is rather small [50,51], as expected.

In the magnetically ordered state, the formula in Eq. (7) is modified as follows:

$$\epsilon = \frac{1}{4} \frac{ceQ_g V_{zz}}{E_\gamma} \left(\frac{3\cos^2\theta - 1}{2} \right), \quad (8)$$

where θ is the angle between the principal component axis of the EFG (c axis in our case) and the direction of Eu hyperfine field B_{hf} and, therefore, the Eu magnetic moment. Hence it is in general possible to obtain information about the orientation of Eu magnetic moments. However, we note that V_{zz} and θ are fitted simultaneously in the same term, Eq. (8), and more than one solution may provide similar fit quality. In order to facilitate the fitting procedure in the ordered state, one could use parameters δ and V_{zz} obtained in the paramagnetic state. Since they are usually temperature dependent, we conducted a measurement just above T_N , i.e., at $T = 30$ K, shown in Fig. 11(b). Compared to room temperature the isomer shift δ somewhat changes and the absolute value of V_{zz} increases as is expected due to the lattice contraction and the corresponding decrease of inter-atomic distances [52].

We note here that there are three recent studies, which discuss possible orientation of Eu magnetic moments in EuZn_2P_2 . Berry *et al.* and Singh *et al.* suggested that there is a planar A-type antiferromagnetic order, i.e., Eu moments lie in the basal plane [6,7], while Krebber *et al.* using resonant x-ray diffraction reported that Eu moments are tilted from the basal plane by an angle of $40^\circ \pm 10^\circ$ [8]. At $T = 4$ K, the ^{151}Eu spectrum consists of groups of peaks, which is due to the presence of a magnetic hyperfine field at the Eu nucleus, related to the magnetic order of Eu moments. Below we discuss results

TABLE II. Parameters obtained from fitting of the spectrum obtained at $T = 4$ K. In the first row all fitting parameters were free, in the second row V_{zz} was fixed to its value at $T = 30$ K, in the third row the angle θ was fixed at 90° , as suggested by Berry *et al.* [6].

$V_{zz} (10^{20} \text{ V/m}^2)$	$\theta (^\circ)$	δ (mm/s)	B_{hf} (T)
-50.3 ± 5.1	61 ± 1	-11.49 ± 0.01	29.99 ± 0.04
-42.6 (fixed)	63 ± 1	-11.49 ± 0.01	29.97 ± 0.04
-15.7 ± 1.6	90 (fixed)	-11.49 ± 0.01	29.83 ± 0.03

of three fitting procedures with focus on V_{zz} and θ , since δ and B_{hf} are the same within the error margin (see Table II). They are also very similar to those obtained for EuZn_2As_2 [9]. First we performed a fit with all parameters free and we obtained $|V_{zz}|$ somewhat larger compared to that at $T = 30$ K, which is expected, and the angle $\theta = 61^\circ$. This fit is shown in Fig. 11(c). In the second attempt we fixed V_{zz} at the value obtained at $T = 30$ K and we obtained the angle $\theta = 63^\circ$. Obtained values of θ indicate that Eu moments are inclined from the basal plane by about 30° , in a good agreement with the value suggested by Krebber *et al.* [8]. In the final fit, we fixed the angle θ at 90° , a value suggested by Berry *et al.*, and we obtained $|V_{zz}|$ almost three times smaller compared to that at 30 K, which is very unlikely, since $|V_{zz}|$ typically increases with decreasing T [50–52], unless there is a structure phase transition, or strong or uneven change of the lattice parameters with temperature. This is practically excluded by the XRD data discussed above, giving the c/a ratio changes with T only by 0.1%, while a and c vary by 0.2% and 0.3%, respectively. Therefore our Mössbauer spectroscopy results indicate that the option with Eu moments in the basal plane is implausible and that they are tilted from the basal plane, as suggested by Krebber *et al.* [8]. We also stress that our $M(H)$ curves in weak magnetic fields show the same behavior as in Ref. [8], while Berry *et al.* [6] mentioned a linear behavior in weak fields. In fact, such disagreement on the orientation of Eu moments is not unusual. It was observed by different groups studying the same compounds, for example, for structurally similar EuZn_2As_2 [9,53,54] or EuSn_2As_2 [25,55]. The angle θ we found here for EuZn_2P_2 is similar to that in EuZn_2As_2 [9] or EuNi_2As_2 [48]. Such an inclination from the basal plane was indicated by *ab initio* calculations assuming for simplicity a ferromagnetic coupling, giving equal Eu moment component on each Cartesian coordinate x, y, z . This yields the inclination from the basal plane 35° , i.e., $\theta = 55^\circ$.

E. Magnetic phase diagram

In Fig. 12, we summarized characteristic transition points that were obtained as follows. Using the Fisher’s method [56] local maxima and minima in $d(\chi T)/dT$ versus T [where χ is either the real part of ac susceptibility $\chi'(T)$ or the dc susceptibility $\chi(T)$ for each magnetic field] were taken as the characteristic transition points (max. in AC Fisher and max. in DC Fisher). The imaginary part of ac susceptibility $\chi''(T)$ for each magnetic field was investigated for local maxima (max. in AC χ''). By taking the minimum in d^2M/dH^2 versus H min. in DC d^2M/dH^2 points were determined. The

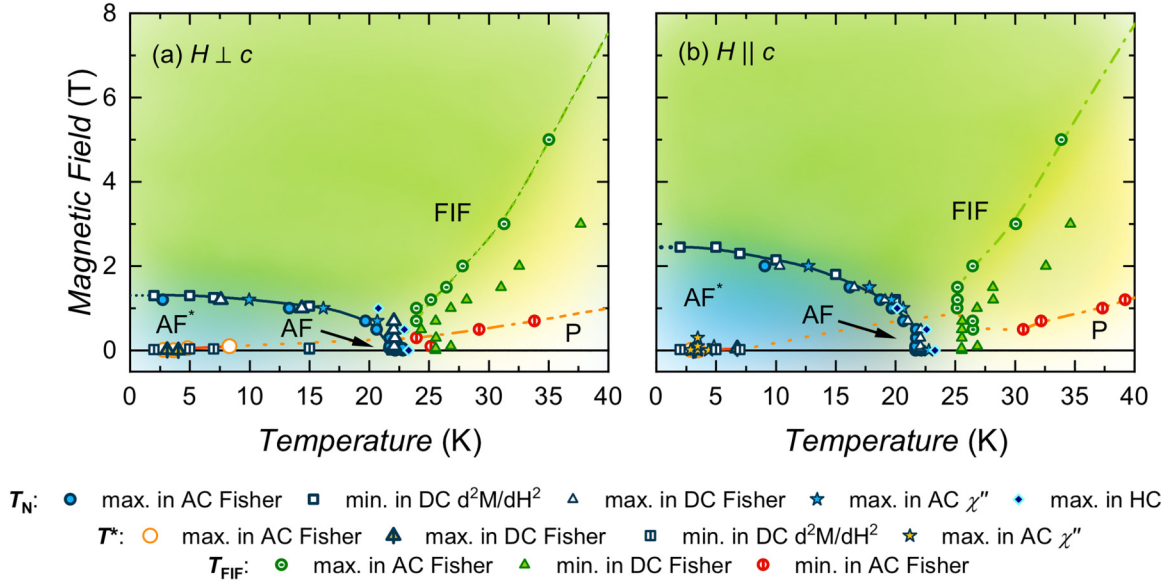


FIG. 12. Magnetic phase diagram of EuZn_2P_2 for magnetic fields applied perpendicular (a) and parallel (b) to the crystallographic c axis. The solid and dashed lines are the guides for the eyes. Abbreviation FIF stands for field induced ferromagnetic.

max. in HC points are corresponding to the maxima in heat capacity $C_p(T)$ for each magnetic field.

Based on these data the magnetic phase diagram was constructed, as a result several phase regions can be distinguished for this compound. As can be seen in Fig. 12 for zero field, going from higher temperatures, a paramagnetic region (P) is followed by a transition at the Néel temperature $T_N = 23$ K to antiferromagnetic order with Eu^{2+} magnetic moments tilted from the basal plane towards the c axis (AF). At lower temperatures (around $T^* = 5$ K), a feature shifting to higher temperatures with increasing field, indicating its origin in ferromagnetic interactions between the Eu^{2+} moments, is visible (AF* region). With application of an external magnetic field another region (field induced ferromagnetic, FIF) can be observed, which is related to the crossover from the paramagnetic state to field induced alignment of the Eu^{2+} magnetic moments below the temperature T_{FIF} .

The observed phenomena indicate that the ground state of EuZn_2P_2 is an antiferromagnet with moments tilted from the basal plane, however there are some additional ferromagnetic features possibly originating from presence of magnetic domains or canted antiferromagnetic order.

F. Magnetoresistance

The temperature dependence of electrical resistivity of EuZn_2P_2 was studied first in Ref. [6]. However, this work covers only a high temperature range (140–400 K). The rapid increase at lower temperatures does not allow to use conventional setups suitable for metallic materials at PPMS systems, as $\text{G}\Omega$ sample resistance is comparable with the resistance of the sample holder without any sample. Here we used an electrometer setup which provides data with reliable temperature dependence as well as absolute values of resistance, which is, however, not easily transformable to resistivity. Very approximately, 1Ω resistance corresponds for the given geometry to $\rho = 10 \text{ m}\Omega\text{cm}$. On the fine scale, the results differed

when changing the range of electrometer, however the orders of magnitude turned out reliable. Figure 13 shows that the resistance increases with decreasing T until it reaches a broad maximum related undoubtedly to magnetism, but located still above the actual T_N . The T_N actually manifests as a minimum, below which resistance resumes its increasing tendency. The position of the broad maximum is very sensitive to magnetic field, being shifted by more than 10 K (from $T_{\text{max}} = 30$ K) in magnetic field of 1 T. The magnetic phase transition temperature is in agreement with the ac susceptibility measurements,

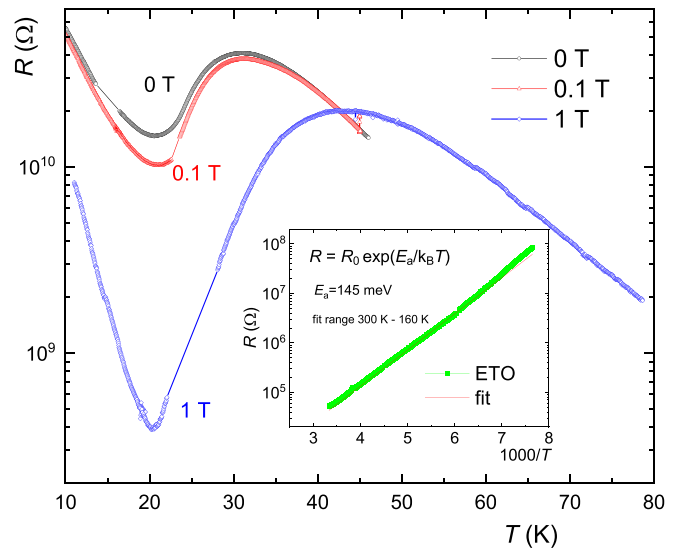


FIG. 13. Temperature dependence of electrical resistance $R(T)$ for current along the basal plane in various magnetic fields applied parallel to the c axis. The inset shows high temperature data in zero field as a function of $1/T$, used to determine the activation energy E_a . The inset data were obtained using the electrical transport option in PPMS (ETO).

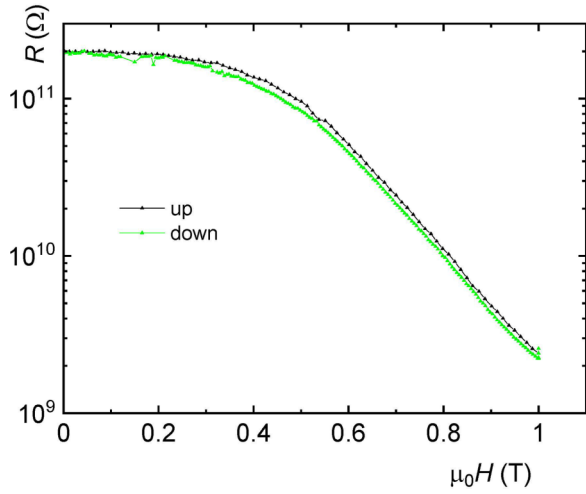


FIG. 14. Magnetoconductance at $T = 10$ K of EuZn_2P_2 for field increasing (black) and decreasing (green). Measurement with current in the basal plane, magnetic field along the c axis.

i.e., shifts slowly to lower temperatures with application of an external magnetic field, reaching 20 K in 1 T. The related minimum gets deeper and sharper.

The high-temperature part of $R(T)$ follows an exponential law with the excitation energy $E_a = 0.145$ eV, which is not far from the value of 0.11 eV reported in Ref. [6]. As $E_g = 2E_a$, the gap width of 290 meV is obtained. As seen, cooling further below the minimum brings another increase of resistance, and values exceeding $10^{11} \Omega$ were recorded at $T = 2$ K. Although this final increase could be ascribed in principle to shallow (2–3 meV) impurity levels in the gap, affecting the electrical conduction, a more simple solution is to assume that the resistivity decrease associated with the antiferromagnetic order, manifested as a band gap reduction, saturates gradually below T_N . Around this temperature, the suppression of magnetic fluctuations can be still assisted by external magnetic field. The field of 1 T is already sufficient to induce the ferromagnetic-like alignment of Eu moments in a limited temperature range. At lower temperatures a phase boundary of the AF state is encountered, which manifests as a sudden termination of the decreasing trend. The field variations in Fig. 13 can be classified as colossal magnetoconductance effects, which are indeed disclosed in Fig. 14, revealing a resistance decrease by two orders of magnitude in $\mu_0H = 1$ T.

G. High pressure studies

Application of hydrostatic pressure leads to a similar effect as magnetic field. The broad maximum of $R(T)$ is gradually shifted towards higher temperatures and absolute R values decrease. In addition, the low- T upturn becomes insignificant. As seen from Fig. 15, the absolute values decrease by many orders of magnitude. The analysis reveals that the activation energy is progressively reduced and the gap disappears at 16–17 GPa. At the highest pressure applied, 18.7 GPa, the sample is apparently in a semimetallic state already, as indicated by $\rho_{300\text{K}} = 8 \text{ m}\Omega \text{ cm}$ and residual resistivity $\rho_0 = 0.5 \text{ m}\Omega \text{ cm}$. Figure 15 shows that even in such case the resistivity in the paramagnetic state is very strongly field dependent, with

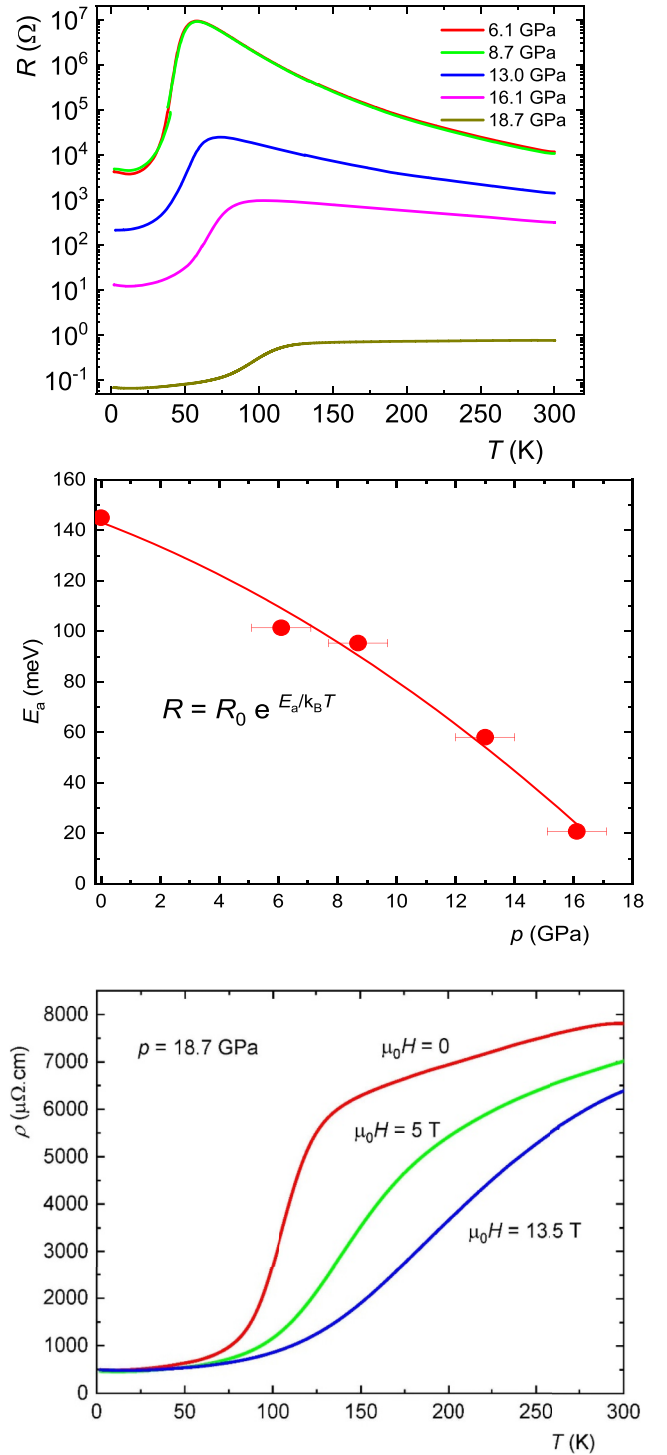


FIG. 15. Variations of $R(T)$ of EuZn_2P_2 as a function of hydrostatic pressure (top). The middle panel describes pressure variations of the gap width. The lower panel displays field variations of resistivity at the highest pressure achieved ($p = 18.7$ GPa), which is sufficient to suppress the gap entirely.

large negative magnetoconductance persisting up to the room temperature. The fact that largest effect is observed around $T = 100$ K, where fields of several Tesla affect magnetic fluctuations, indicates the strong coupling of such fluctuations to the pool of conduction electrons. Such an effect is

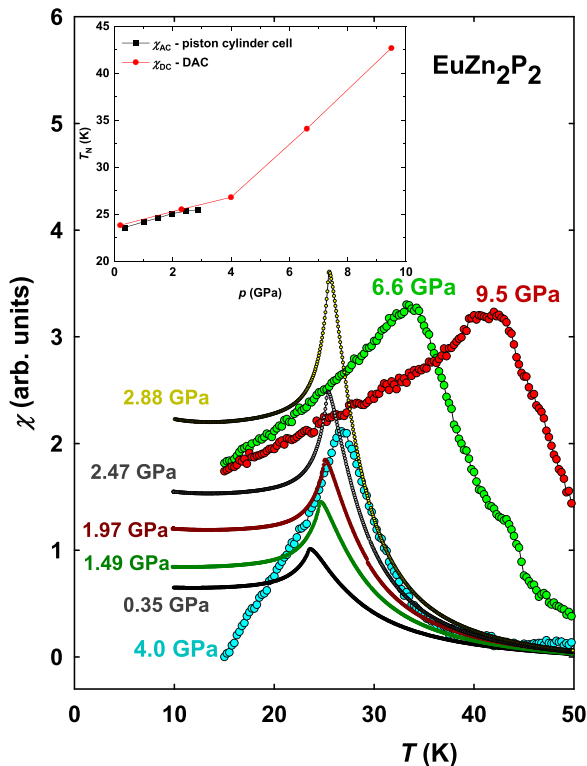


FIG. 16. Pressure variations of magnetic susceptibility of EuZn_2P_2 monitored by *ac* susceptibility in the piston cylinder cell (small points) and dc susceptibility in DAC (large points). The dc susceptibility was measured in the field of 0.01 T. The $\chi(T)$ values were rescaled arbitrarily. The inset displays the pressure dependence of T_N obtained by the two techniques.

necessarily reduced with increasing T , as the thermal energy $k_B T$ becomes much higher than the Zeeman energy of a single Eu moment in given fields.

As shown above, T_N corresponds at ambient pressure to a minimum in $R(T)$, however, the character of $R(T)$ dramatically changes when pressure is applied and from $R(T)$ it is not obvious what is the pressure variation of T_N . Therefore it was essential to determine the susceptibility under pressure. In Fig. 16, two types of experimental results under pressure are displayed. The *ac* susceptibility, $\chi_{ac}(T)$, used in the lower pressure range (up to 3 GPa), provides good hydrostaticity and low noise. The range up to 10 GPa was covered by the dc magnetization measurements. The fact that susceptibility forms a maximum means that the AF order does not transform to ferromagnetism in the pressure range studied. In the range where both techniques overlap we observed their good agreement, following approximately linear increase. This increase becomes steeper around $p = 4$ GPa. The data suggest that there may be another linear increase above this limit, but a more detailed study has to be undertaken to be conclusive. The important fact is that the T_N values at elevated pressures do not correlate with any particular anomaly in $R(T)$. The maximum in $R(T)$ in Fig. 15, albeit related to magnetism, is located above the actual T_N at corresponding pressures. Hence, we tend to associate the maximum, or better the decrease of R

from the exponentially increasing tendency, with magnetic fluctuations, inducing magnetic polarons.

As the family of ternary Eu Zintl phases with a distinctly layered structure is quite extended, we can compare the behavior with other systems, having identical or very similar crystal structure. For some of them, even the pressure variations of the behavior have been explored. A convenient starting point of understanding is that the Eu magnetism implies the $4f^7 5d^0$ (Eu^{2+}) state. This charge state is at least to some extent robust against the lattice compression. On the other hand, the state with $4f^6 5d^1$ configuration has dramatically lower volume and should be therefore preferred in a highly compressed state. The $4f^6$ state with $L = S = 3, J = L - S = 0$ is naturally non magnetic. In addition, valence fluctuations between one magnetic and one non-magnetic state may also produce non-magnetic ground state due to the dynamics of charge fluctuations or Kondo effect. For systems tunable across the loss of magnetism either by changes of composition or pressure, as, e.g., $\text{Eu}(\text{Rh}_{1-x}\text{Ir}_x)_2\text{Si}_2$, the transition can be of the first order type [57].

A characteristic feature of electronic structure of the Eu Zintl phases (those containing a pnictogen or chalcogen) is existence of a gap at the Fermi level, with the $3p$ states of P contributing to the upper edge of the valence band and $5d$ states of Eu in the conduction band.

For EuZn_2P_2 , the pressure induced gradual gap suppression, indicated both by calculations and resistivity studies, can thus eventually bring the $5d$ states to and below the Fermi level. We can speculate then that a crossing of the metal insulator transition giving a fractional occupancy of the $5d$ states may also give a non-magnetic state due to the mean $4f$ occupancy sinking below 7, which would suppress its magnetism. In pressures used here, EuZn_2P_2 , is however still on the ascending part of the dependence of T_N on pressure. It implies that the $4f$ occupancy stays at 7 and the effective inter-site exchange coupling increases. As pointed out already for various isostructural compounds [6], the Eu-Eu distances are likely the explicit tuning parameter. This is, however, true both for the dipole-dipole interaction suggested in Ref. [6] and (more likely) for the superexchange, depending on the $4f$ - $3p$ hybridization. The observed increase of T_N of EuZn_2P_2 under pressure is the continuation of the same trend to even smaller distances than available compounds offer within the same structure type. What remains to complete the story is to describe the pressure variations of lattice parameters. The anisotropy of lattice thermal expansion detected here for EuZn_2P_2 , suggests that also individual compressibilities under hydrostatic pressure may exhibit a significant anisotropy.

Such robust enhancement of ordering temperatures in Eu systems is naturally not restricted to the given family of ternaries. As a simple model systems one can take, e.g., Eu monochalcogenides, which crystallize in the cubic rocksalt structure. Indeed, magnetic ordering temperatures increase with decreasing size of a chalcogen or with pressure. Moreover, the gradual compression turns the antiferromagnetic order of EuTe into ferromagnet, with the critical Eu spacing around 5.2 Å, achieved in ≈ 8 GPa [58]. On the other side of the series, EuO with the ferromagnetic ground state has T_C dramatically increasing by 5 K/GPa [59] from 69.2 K at ambient pressure. A remarkable fact is that both the

predominance of the F order at low Eu-Eu distances and increase of T_C with compression are well accounted by *ab initio* calculations (LDA + U). [60] An analysis shows an important role of the p - f mixing and superexchange. With such background information it is understandable that the exchange in the basal plane is strong and ferromagnetic, as the Eu-Eu distances are far below 5 Å, while much longer bonds along the c axis bring AF coupling, which is so weak that it can be broken in magnetic fields of few tesla. The superexchange operates, as pointed out in Ref. [7], via the P atoms adjacent to the Eu planes. The situation with strong in-plane coupling and weak inter-plane one brings 2D magnetic correlations existing above T_N . Their footprint can be seen in magnetic entropy extending up to $T = 40$ K even in zero magnetic field.

Among compounds with the same crystal structure, EuZn_2As_2 with lattice parameters somewhat higher and $T_N = 19.2$ K lower than for EuZn_2P_2 , exhibits a remarkable similarity to EuZn_2P_2 [9]. While there are no high pressure data for EuZn_2As_2 , high pressure effects were studied for EuIn_2As_2 with a similar structure type [3]. It is more metallic than EuZn_2P_2 , possibly with a very narrow gap around the Γ point, at which nontrivial topologically protected states are present at the Fermi energy E_F . As those states depend on the symmetry imposed by magnetic ordering, any moments reorientation yields a large impact on electrical resistivity. A complicated helicoidal magnetic structure of the ground state makes the situation quite involved [61]. The impact of pressure is very dramatic. The T_N value increases up to 65 K in $p = 14.7$ GPa, which is attributed to stronger exchange coupling in the basal plane. In pressures exceeding 17 GPa it becomes amorphous and metallic, so the trend could not be followed continuously any more [3]. We can think about the first order transition coupling the volume collapse with the valence change. The amorphization can appear in the situation in which a local structure motif imposed by bonding conditions modified by the compression is incompatible with the 3D translation periodicity of the crystal lattice. An interesting feature is rather low bulk modulus $B_0 = 32.3$ GPa. Comparing the linear compressibilities from the data in Ref. [3], one can deduce that the c axis is actually much softer. Increasing pressure brings metallization seen in electrical resistivity, while the colossal magnetoresistance effect is gradually suppressed. Although topological states depending on the symmetry of the AF state turning to F under the influence of field can affect the resistivity, a general and more simple mechanism is a reduction of the band gap. Even if it happens for one spin direction only, a simple parallel resistor model reveals that the opposite spin direction where the gap increases becomes for conduction practically irrelevant. The other side of the coin is that the conduction electrons are very strongly spin polarized, which gives rise to a spin filter effect, described, e.g., for EuO [62]. An interesting fact is that the largest magnetoresistance effect is for EuZn_2P_2 recorded not in the low temperature limit, but above T_N , where the resistance forms a pronounced knee. Evidently the strong coupling of transport to magnetic fields reflects the field effect on magnetic correlations above T_N . In particular, we can expect magnetic field to have a stabilizing effect on ferromagnetic fluctuations, assumed within the basal

plane. As we measure, due to the geometry of the crystals grown, the resistivity perpendicular to the c axis, the experiment is particularly sensitive to the correlations in the basal plane. Applying pressure the knee shifts accordingly, exceeding $T = 100$ K. The largest magnetoresistance point shifts to ≈ 150 K. The fact that there is very little field dependence in the low- T limit can mean that the type of order actually changes from AF to F in the higher pressures applied in this work.

IV. SUMMARY AND CONCLUSIONS

EuZn_2P_2 is an antiferromagnetic layered compound with a narrow band gap, which is intimately connected with the magnetic state. We assume a strong ferromagnetic Eu-Eu exchange coupling within the basal plane sheets, based on superexchange including phosphorus ions. The weaker interaction to more remote Eu neighbours along the c axis is antiferromagnetic, which determines the type of magnetic order. The Eu^{2+} moments are inclined from the basal plane. Large Eu moments of $7 \mu_B$, weak AF coupling and very weak magnetocrystalline anisotropy (Eu^{2+} has spin-only moments similar to Gd^{3+} , but absence of $5d$ occupancy makes the anisotropy even weaker than for Gd systems) facilitate the rotation of moments into a field aligned state, accomplished in $\mu_0 H = 2$ T. This dramatically reduces resistivity not only in the AF state but also above T_N . Such CMR effect is even more pronounced in a limited T range above the actual T_N , which is related to ferromagnetic correlations. The phenomenon can be related to the reduction of the gap width. The gap is suppressed in $p \approx 17$ GPa, where EuZn_2P_2 becomes a semi-metal, probably ferromagnetic. Hence we can anticipate that it is also a half-metal with one spin direction only at the Fermi level. Hydrostatic pressure also increases T_N from 23 K to almost 45 K in $p = 10$ GPa, which seems to be quite general effect for Eu systems with a band gap [59]. As the crystal structure does not have a center of symmetry, further research will have to focus on possible non-trivial topological states and their interplay with the symmetry of magnetic state and its development in magnetic fields.

ACKNOWLEDGMENTS

D.R. acknowledges financial support by National Science Centre, Poland (Grant No. 2018/30/E/ST3/00377). W.T. and K.K. acknowledge the support of the National Science Centre, Poland, Grant No. OPUS: 2021/41/B/ST3/03454. Research project was partly supported by program “Excellence initiative—research university” for the AGH University of Krakow. The work has been supported by the Czech Science Foundation under the Grants No. 21-09766S and No. 22-22322S (D.L.). D.L. also acknowledges the computational resources by project e-INFRA CZ (ID:90254) and project QM4ST CZ.02.01.01/00/22_008/0004572 both by the Ministry of Education, Youth and Sports of the Czech Republic. Some experiments were performed in MGML (mgml.eu), which is supported within the program of the Czech Research Infrastructures (Project No. LM2023065).

- [1] S. M. Kauzlarich, Zintl phases: From curiosities to impactful materials, *Chem. Mater.* **35**, 7355 (2023).
- [2] C. Zheng and R. Hoffmann, Complementary local and extended views of bonding in the ThCr_2Si_2 and CaAl_2Si_2 structures, *J. Solid State Chem.* **72**, 58 (1988).
- [3] F. H. Yu, H. M. Mu, W. Z. Zhuo, Z. Y. Wang, Z. F. Wang, J. J. Ying, and X. H. Chen, Elevating the magnetic exchange coupling in the compressed antiferromagnetic axion insulator candidate EuIn_2As_2 , *Phys. Rev. B* **102**, 180404(R) (2020).
- [4] S. Luo, Y. Xu, F. Du, L. Yang, Y. Chen, C. Cao, Y. Song, and H. Yuan, Colossal magnetoresistance and topological phase transition in EuZn_2As_2 , *Phys. Rev. B* **108**, 205140 (2023).
- [5] X. Chen, S. Wang, J. Wang, C. An, Y. Zhou, Z. Chen, X. Zhu, Y. Zhou, Z. Yang, and M. Tian, Temperature-pressure phase diagram of the intrinsically insulating topological antiferromagnet EuCd_2As_2 , *Phys. Rev. B* **107**, L241106 (2023).
- [6] T. Berry, V. J. Stewart, B. W. Y. Redemann, C. Lygouras, N. Varnava, D. Vanderbilt, and T. M. McQueen, A-type antiferromagnetic order in the Zintl-phase insulator EuZn_2P_2 , *Phys. Rev. B* **106**, 054420 (2022).
- [7] K. Singh, S. Dan, A. Ptok, T. A. Zaleski, O. Pavlosiuk, P. Wiśniewski, and D. Kaczorowski, Superexchange interaction in insulating EuZn_2P_2 , *Phys. Rev. B* **108**, 054402 (2023).
- [8] S. Krebber, M. Kopp, C. Garg, K. Kummer, J. Sichelschmidt, S. Schulz, G. Poelchen, M. Mende, A. V. Virovets, K. Warawa, M. D. Thomson, A. V. Tarasov, D. Y. Usachov, D. V. Vyalikh, H. G. Roskos, J. Müller, C. Krellner, and K. Kliemt, Colossal magnetoresistance in EuZn_2P_2 and its electronic and magnetic structure, *Phys. Rev. B* **108**, 045116 (2023).
- [9] Z. Bukowski, D. Rybicki, M. Babij, J. Przewoźnik, Ł. Gondek, J. Żukrowski, and C. Kapusta, Canted antiferromagnetic order in EuZn_2As_2 single crystals, *Sci. Rep.* **12**, 14718 (2022).
- [10] See Supplemental Material at <http://link.aps.org/supplemental/10.1103/PhysRevB.110.014421> for photo of crystals, more details on the experimental data, and experimental and calculations methods.
- [11] J. Rodríguez-Carvajal, Recent advances in magnetic structure determination by neutron powder diffraction, *Phys. B: Condens. Matter* **192**, 55 (1993).
- [12] N. Fujiwara, T. Matsumoto, K. Nakazawa, A. Hisada, and Y. Uwatoko, Fabrication and efficiency evaluation of a hybrid NiCrAl pressure cell up to 4 GPa, *Rev. Sci. Instrum.* **78**, 073905 (2007).
- [13] K. Murata, K. Yokogawa, H. Yoshino, S. Klotz, P. Munsch, A. Irizawa, M. Nishiyama, K. Iizuka, T. Nanba, T. Okada, Y. Shiraga, and S. Aoyama, Pressure transmitting medium Daphne 7474 solidifying at 3.7 GPa at room temperature, *Rev. Sci. Instrum.* **79**, 085101 (2008).
- [14] D. Staško, J. Prchal, M. Klicpera, S. Aoki, and K. Murata, Pressure media for high pressure experiments, Daphne oil 7000 series, *High Press. Res.* **40**, 525 (2020).
- [15] G. Giriat, W. Wang, J. P. Attfield, A. D. Huxley, and K. V. Kamenev, Turnbuckle diamond anvil cell for high-pressure measurements in a superconducting quantum interference device magnetometer, *Rev. Sci. Instrum.* **81**, 073905 (2010).
- [16] K. Parlinski, Z. Q. Li, and Y. Kawazoe, First-principles determination of the soft mode in cubic ZrO_2 , *Phys. Rev. Lett.* **78**, 4063 (1997).
- [17] A. Togo, L. Chaput, I. Tanaka, and G. Hug, First-principles phonon calculations of thermal expansion in Ti_3SiC_2 , Ti_3AlC_2 , and Ti_3GeC_2 , *Phys. Rev. B* **81**, 174301 (2010).
- [18] A. Togo, L. Chaput, and I. Tanaka, Distributions of phonon lifetimes in Brillouin zones, *Phys. Rev. B* **91**, 094306 (2015).
- [19] F. Sayetat, P. Fertey, and M. Kessler, An easy method for the determination of Debye temperature from thermal expansion analyses, *J. Appl. Crystallogr.* **31**, 121 (1998).
- [20] N. Ashcroft and N. D. Mermin, *Solid State Physics* (Harcourt College Publishers, Fort Worth, 1976).
- [21] L. Gondek, A. Szytuła, D. Kaczorowski, A. Szewczyk, M. Gutowska, and P. Piekarczyk, Multiple magnetic phase transitions in $\text{Tb}_3\text{Cu}_4\text{Si}_4$, *J. Phys.: Condens. Matter* **19**, 246225 (2007).
- [22] V. K. Anand and D. C. Johnston, Antiferromagnetism in EuCu_2As_2 and $\text{EuCu}_{1.82}\text{Sb}_2$ single crystals, *Phys. Rev. B* **91**, 184403 (2015).
- [23] S. Pakhira, M. A. Tanatar, and D. C. Johnston, Magnetic, thermal, and electronic-transport properties of EuMg_2Bi_2 single crystals, *Phys. Rev. B* **101**, 214407 (2020).
- [24] N. S. Sangeetha, S. Pakhira, D. H. Ryan, V. Smetana, A.-V. Mudring, and D. C. Johnston, Magnetic phase transitions in $\text{Eu}(\text{Co}_{1-x}\text{Ni}_x)_2\text{As}_2$ single crystals, *Phys. Rev. Mater.* **4**, 084407 (2020).
- [25] S. Pakhira, M. A. Tanatar, T. Heitmann, D. Vaknin, and D. C. Johnston, A-type antiferromagnetic order and magnetic phase diagram of the trigonal Eu spin- $\frac{7}{2}$ triangular-lattice compound EuSn_2As_2 , *Phys. Rev. B* **104**, 174427 (2021).
- [26] S. Pakhira, F. Islam, E. O'Leary, M. A. Tanatar, T. Heitmann, L.-L. Wang, R. Prozorov, A. Kaminski, D. Vaknin, and D. C. Johnston, A-type antiferromagnetic order in semiconducting EuMg_2Sb_2 single crystals, *Phys. Rev. B* **106**, 024418 (2022).
- [27] S. Pakhira, A. K. Kundu, F. Islam, M. A. Tanatar, T. Roy, T. Heitmann, T. Yilmaz, E. Vescovo, M. Tsujikawa, M. Shirai, R. Prozorov, D. Vaknin, and D. C. Johnston, Anisotropic magnetism and electronic structure of trigonal EuAl_2Ge_2 single crystals, *Phys. Rev. B* **107**, 134439 (2023).
- [28] M. Giovannini, I. Čurlík, R. Freccero, P. Solokha, M. Reiffers, and J. Sereni, Crystal structure and magnetism of noncentrosymmetric $\text{Eu}_2\text{Pd}_2\text{Sn}$, *Inorg. Chem.* **60**, 8085 (2021).
- [29] K. A. Gschneidner, V. K. Pecharsky, and A. O. Tsokol, Recent developments in magnetocaloric materials, *Rep. Prog. Phys.* **68**, 1479 (2005).
- [30] K. Ahn, A. O. Pecharsky, K. A. Gschneidner, Jr., and V. K. Pecharsky, Preparation, heat capacity, magnetic properties, and the magnetocaloric effect of EuO , *J. Appl. Phys.* **97**, 063901 (2005).
- [31] L. M. Tran, M. Babij, L. Korosec, T. Shang, Z. Bukowski, and T. Shiroka, Magnetic phase diagram of Ca-substituted EuFe_2As_2 , *Phys. Rev. B* **98**, 104412 (2018).
- [32] I. Turek, V. Drchal, J. Kudrnovský, M. Sob, and P. Weinberger, *Electronic Structure of Disordered Alloys, Surfaces and Interfaces* (Kluwer Academic Publishers, Boston, 1997).
- [33] M. Pajda, J. Kudrnovský, I. Turek, V. Drchal, and P. Bruno, Oscillatory Curie temperature of two-dimensional ferromagnets, *Phys. Rev. Lett.* **85**, 5424 (2000).
- [34] I. Turek, J. Kudrnovsky, V. Drchal, and P. Bruno, Exchange interactions, spin waves, and transition temperatures in itinerant magnets, *Philos. Mag.* **86**, 1713 (2006).

- [35] A. I. Liechtenstein, M. I. Katsnelson, V. P. Antropov, and V. A. Gubanov, Local spin density functional approach to the theory of exchange interactions in ferromagnetic metals and alloys, *J. Magn. Magn. Mater.* **67**, 65 (1987).
- [36] H. Eschrig, K. Koepnick, and I. Chaplygin, Density functional application to strongly correlated electron systems, *J. Solid State Chem.* **176**, 482 (2003).
- [37] G. Kresse and J. Furthmüller, Efficient iterative schemes for *ab initio* total-energy calculations using a plane-wave basis set, *Phys. Rev. B* **54**, 11169 (1996).
- [38] P. E. Blöchl, Projector augmented-wave method, *Phys. Rev. B* **50**, 17953 (1994).
- [39] G. Kresse and D. Joubert, From ultrasoft pseudopotentials to the projector augmented-wave method, *Phys. Rev. B* **59**, 1758 (1999).
- [40] J. P. Perdew, K. Burke, and M. Ernzerhof, Generalized gradient approximation made simple, *Phys. Rev. Lett.* **77**, 3865 (1996).
- [41] K. Koepnick and H. Eschrig, Full-potential nonorthogonal local-orbital minimum-basis band-structure scheme, *Phys. Rev. B* **59**, 1743 (1999).
- [42] A. I. Liechtenstein, V. I. Anisimov, and J. Zaanen, Density-functional theory and strong interactions: Orbital ordering in Mott-Hubbard insulators, *Phys. Rev. B* **52**, R5467 (1995).
- [43] V. H. Tran, Z. Bukowski, L. M. Tran, and A. J. Zaleski, The electronic phase diagrams of the $\text{Eu}(\text{Fe}_{0.81}\text{Co}_{0.19})_2\text{As}_2$ superconductor, *New J. Phys.* **14**, 073052 (2012).
- [44] L. M. Tran, A. J. Zaleski, and Z. Bukowski, Reentrant resistivity due to the interplay of superconductivity and magnetism in $\text{Eu}_{0.73}\text{Ca}_{0.27}(\text{Fe}_{0.87}\text{Co}_{0.13})_2\text{As}_2$, *Phys. Rev. B* **109**, 014509 (2024).
- [45] S. Zapf, C. Stingl, K. W. Post, J. Maiwald, N. Bach, I. Pietsch, D. Neubauer, A. Löhle, C. Clauss, S. Jiang, H. S. Jeevan, D. N. Basov, P. Gegenwart, and M. Dressel, Persistent detwinning of iron-pnictide EuFe_2As_2 crystals by small external magnetic fields, *Phys. Rev. Lett.* **113**, 227001 (2014).
- [46] I. Schellenberg, M. Eul, W. Hermes, and R. Pöttgen, A ^{121}Sb and ^{151}Eu Mössbauer spectroscopic investigation of EuMn_2Sb_2 , EuZn_2Sb_2 , YbMn_2Sb_2 , and YbZn_2Sb_2 , *Z. Anorg. Allg. Chem.* **636**, 85 (2010).
- [47] A. Błachowski, K. Ruebenbauer, J. Żukrowski, Z. Bukowski, K. Rogacki, P. J. W. Moll, and J. Karpinski, Interplay between magnetism and superconductivity in $\text{EuFe}_{2-x}\text{Co}_x\text{As}_2$ studied by ^{57}Fe and ^{151}Eu Mössbauer spectroscopy, *Phys. Rev. B* **84**, 174503 (2011).
- [48] K. Komędera, A. Gatlik, A. Błachowski, J. Żukrowski, D. Rybicki, A. Deleka, M. Babij, and Z. Bukowski, ^{57}Fe and ^{151}Eu Mössbauer studies of 3d-4f spin interplay in $\text{EuFe}_{2-x}\text{Ni}_x\text{As}_2$, *Sci. Rep.* **11**, 11484 (2021).
- [49] Y. Yoshida and G. Langouche, *Mössbauer Spectroscopy* (Springer-Verlag, Berlin, Heidelberg, 2013).
- [50] M. A. Albedah, F. Nejadattari, Z. M. Stadnik, Y. Liu, and G.-H. Cao, Mössbauer spectroscopy measurements on the 35.5 K superconductor $\text{Rb}_{1-\delta}\text{EuFe}_4\text{As}_4$, *Phys. Rev. B* **97**, 144426 (2018).
- [51] M. A. Albedah, Z. M. Stadnik, O. Fedoryk, Y.-B. Liu, and G.-H. Cao, Magnetic properties of EuFeAs_2 and the 14 K superconductor $\text{EuFe}_{0.97}\text{Ni}_{0.03}\text{As}_2$, *J. Magn. Magn. Mater.* **503**, 166603 (2020).
- [52] D. Torumba, K. Parlinski, M. Rots, and S. Cottenier, Temperature dependence of the electric-field gradient in hcp-Cd from first principles, *Phys. Rev. B* **74**, 144304 (2006).
- [53] J. Blawat, M. Marshall, J. Singleton, E. Feng, H. Cao, W. Xie, and R. Jin, Unusual electrical and magnetic properties in layered EuZn_2As_2 , *Adv. Quantum Technol.* **5**, 2200012 (2022).
- [54] E. Yi, D. F. Zheng, F. Pan, H. Zhang, B. Wang, B. Chen, D. Wu, H. Liang, Z. X. Mei, H. Wu, S. A. Yang, P. Cheng, M. Wang, and B. Shen, Topological Hall effect driven by short-range magnetic order in EuZn_2As_2 , *Phys. Rev. B* **107**, 035142 (2023).
- [55] H. Li, S.-Y. Gao, S.-F. Duan, Y.-F. Xu, K.-J. Zhu, S.-J. Tian, J.-C. Gao, W.-H. Fan, Z.-C. Rao, J.-R. Huang, J.-J. Li, D.-Y. Yan, Z.-T. Liu, W.-L. Liu, Y.-B. Huang, Y.-L. Li, Y. Liu, G.-B. Zhang, P. Zhang, T. Kondo *et al.*, Dirac surface states in intrinsic magnetic topological insulators EuSn_2As_2 and $\text{MnBi}_{2n}\text{Te}_{3n+1}$, *Phys. Rev. X* **9**, 041039 (2019).
- [56] M. E. Fisher, Relation between the specific heat and susceptibility of an antiferromagnet, *Philos. Mag.* **7**, 1731 (1962).
- [57] S. Seiro and C. Geibel, Divalent to valence-fluctuating behaviour in $\text{Eu}(\text{Rh}_{1-x}\text{Ir}_x)_2\text{Si}_2$ single crystals, *J. Phys.: Condens. Matter* **23**, 375601 (2011).
- [58] M. Ishizuka, Y. Kai, R. Akimoto, M. Kobayashi, K. Amaya, and S. Endo, Pressure-induced ferromagnetism in EuTe , *J. Magn. Magn. Mater.* **166**, 211 (1997).
- [59] R. Stevenson and M. Robinson, Effect of pressure on ferromagnetic phase transition of EuO , *Can. J. Phys.* **43**, 1744 (1965).
- [60] J. Kunes, W. Ku, and W. E. Pickett, Exchange coupling in Eu monochalcogenides from first principles, *J. Phys. Soc. Jpn.* **74**, 1408 (2005).
- [61] S. X. M. Riberolles, T. Trevisan, B. Kuthanazhi, T. W. Heitmann, F. Ye, D. C. Johnston, S. L. Bud'ko, D. H. Ryan, P. C. Canfield, A. Kreyssig, A. Vishwanath, R. J. McQueeney, L.-L. Wang, P. P. Orth, and B. G. Ueland, Magnetic crystalline-symmetry-protected axion electrodynamics and field-tunable unpinned Dirac cones in EuIn_2As_2 , *Nat. Commun.* **12**, 999 (2021).
- [62] N. Jutong, I. Rungger, C. Schuster, U. Eckern, S. Sanvito, and U. Schwingenschloegl, Electronic transport through EuO spin-filter tunnel junctions, *Phys. Rev. B* **86**, 205310 (2012).